Faculty Applied Sciences

A linear stability analysis of a water loop driven by natural convection at supercritical conditions

D. Krijger, July 2013

NERA-131-2013-004

Naam:	Dennis Krijger		
Studentnummer:	4081552		
Opleiding:	Technische Natuurkunde		
Begeleider:	Martin Rohde	**Sectie:**	NERA
2de beoordelaar:	Erik van der Kolk		
Startdatum:	22-04-2013	**Einddatum:**	17-07-2013
Is vertrouwelijkheid van toepassing?	Nee		

NOMENCLATURE

Roman characters

A	m^2	flow area
D_h	m	hydraulic diameter
f		friction factor
g	$m\ s^{-2}$	gravity acceleration
H	$J\ kg^{-1}$	specific enthalpy
h	$J\ kg^{-1}$	specific enthalpy
K		pressure loss coefficient
L	m	length (without subscript: length of core)
p	Pa	pressure
Q	$J\ s^{-1}$	heating power of the core
q	$J\ s^{-1}$	heat loss
S	m	perimeter pipe
t	s	time
u	$m\ s^{-1}$	streamwise velocity
V	m^3	volume
W	$kg\ s^{-1}$	mass flow rate

Greek characters

μ	Pa s	dynamic viscosity
ϑ	rad	angle
λ		eigenvalue
ρ	$kg\ m^{-3}$	density
τ	Pa	shear stress
υ	$m^3\ kg^{-1}$	specific volume

Subscripts

0	value lower part of the core
1	value at upper part of the core
B	value at buffer vessel
D	value at downcomer
IN	value at inlet at the core
out	value at core outlet
pc	value at the pseudo-critical point
R	value at riser

Dimensionless numbers

N_{Fr}	Froude number
N_{sub}	Subcooling-Number
$N_{\Delta h}$	Pseudo-Phase-Change-Number
Re	Reynolds number

Other

$\underset{\sim}{x}$	dimensionless variable
$\overline{X}$	steady state variable
$\breve{x}$	perturbation if lowercase is not available

Abbreviations

BWR	Boiling Water Reactor
ESBWR	Economic Simplified Boiling Water Reactor
HPLWR	High Performance Light Water Reactor
NSB	Neutral Stability Boundary
RPV	Reactor Pressure Vessel
SCWR	Supercritical Water Reactor

ABSTRACT

This thesis focuses on the stability of the European High Performance Light Water Reactor (HPLWR). The HPLWR design is based on the Supercritical Water Reactor concept (SCWR), which is one of the six Generation IV reactor concepts. This reactor is designed to facilitate safer operation, operate more efficient and environmentally friendly. The efficiency of a HPLWR is estimated to be 44% and this becomes among other things possible due to the high temperatures of the supercritical water. One way to enhance the safety of this reactor is to eliminate the need for pumps to drive the circulation of the water, an idea based on the Economic Simplified Boiling Water Reactor (ESBWR). Such a feature may introduce additional stability issues, which need to be investigated first.

The stability of the whole system in this water loop driven by natural convection is investigated with a linear analysis. Two simplified water loop models have been developed and the conservation balances have been set up accordingly and linearized. The stability problem is solved by investigating the response of the system to introduced perturbations. Stability maps were derived for a range of operating conditions and investigated. A parametric study was performed to study the influence of various design parameters. The length of the riser turns out to be an important design parameter, because increasing the length destabilizes the system and on the other hand increases the mass flow rate. Consideration must go into the trade-off between a stable system and a sufficient mass flow rate. Also frequency maps were derived that give more insight into the type of instabilities occurring in the system. Finally, a method is proposed to find Ledinegg unstable regions in the stability maps for natural circulation driven systems. Ledinegg unstable regions were found in this research, but their position within the stability map could not be exactly predicted.

CONTENTS

Nomenclature i
Abstract iii
Contents iv
1 Introduction 1
1.1 Background of research 1
1.2 Supercritical water 3
1.3 The stability problem 5
1.4 Literature survey 6
1.5 Outline 7
2 Mathematical foundation 9
2.1 The High Performance Light Water Reactor 9
2.2 Simplification of the HPLWR 11
2.2.1 The equation of state 11
2.2.2 Geometry 12
2.3 The water loop model 14
2.4 The low heating model 15
2.4.1 Conservation balances 15
2.4.2 Reduction of variables and equations 18
2.4.3 Dimensionless balances 18
2.4.4 Linearized conservation balances 19
2.5 The high heating model 22
2.5.1 Conservation balances 22
2.5.2 Reduction of variables and equations 24
2.5.3 Dimensionless balances 24
2.5.4 Linearized conservation balances 25
3 Investigating the stability 27
3.1 The matrix equation 27
3.2 Solving for lambda 28
3.3 Dimensionless numbers 28

4 Computational implementation 31
4.1 Overall considerations 31
4.2 The code 31
4.2.1 The general algorithm 31
4.2.2 The steady state solutions of the enthalpy and length of node 1 32
4.2.3 The steady state mass flow rate 33
4.2.4 The eigenvalue problem 34
4.3 Resonance frequencies 34
4.4 Ledinegg instabilities 35
5 Results 39
5.1 Parametric study 39
5.1.1 Reference case 40
5.1.2 Volume of the buffer vessel 41
5.1.3 Riser length 42
5.1.4 Length core and hydraulic diameter 44
5.1.5 Outlet and inlet restrictions 45
5.2 Ledinegg instability 46
6 Conclusions 51
6.1 Conclusions 51
6.2 Discussion 52
Bibliography 53
Appendix A 56
Appendix B 58

1 INTRODUCTION

1.1 BACKGROUND OF RESEARCH

With an ever increasing consumption of energy by the average world citizen reliable energy sources are becoming more important than ever. Due to the well-known effects of fossil fuel burning, emission of huge amounts of CO_2 in the atmosphere, clean energy sources are key for a sustainable future. Therefore, research is more focusing on enhancing the nuclear reactors of this time. The nuclear reactors that are planned for construction or those which are currently under construction are mostly Generation III reactor types. However, a lot of scientists are nowadays researching the concept of a Generation IV reactor, which should be substantially more environmentally friendly, economical, efficient and support safer operation than the Generation III reactor type (Ortega Gómez, 2009).

One of the Generation IV reactor concepts is the supercritical water reactor (SCWR), on which the aim of this thesis lies. The working fluid is water which serves as the coolant and as the moderator. This reactor operates under a high pressure with high temperatures. The pressure and outlet temperature lie above the critical point of water. This topic is further explained in section 1.2. A reactor based on the SCWR concept is also referred to as a High Performance Light Water Reactor (HPLWR). Research into this reactor, called the HPLWR Phase 2 project, is done by a consortium of 10 partners from 8 European countries funded by the European Commission. One of the unique design features of this reactor is its core configuration, see Figure 1.1. Water flows into the core in the upwards direction and heats up in three stages. Between these three stages mixing chambers are placed for a homogenous temperature distribution of the coolant. This three-pass core design provides uniform heating and prevents hotspots in the core (Ortega Gómez, 2009).

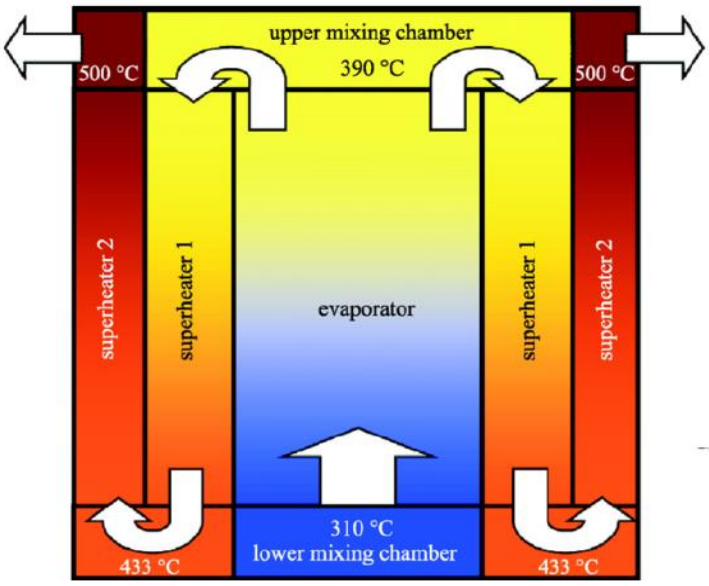

Figure 1.1: A three-pass core design that provides uniform heating and prevents hotspots. The intermediate mixing chambers provide a homogenous temperature distribution. Source: (Fischer, Schulenberger, & Laurien, 2009).

The HPLWR operates under a pressure of 25 MPa and has a projected electrical power output of 1000 MW (Schulenberg, et al., 2011). The main reason why supercritical water is used is the increased efficiency that becomes theoretically possible due to the higher outlet temperatures that can be reached. The outlet temperature of the water lies around 500°C (Ortega Gómez, 2009). Also as the water reaches a certain temperature, called the pseudo-critical temperature, the specific heat capacity increases significantly and the coolant can carry more heat from the core to the turbines without a large increase of temperature (see Figure 1.4). With a HPLWR an efficiency of approximately 44% can be achieved, in contrast with an efficiency of 33% with a Boiling Water Reactor (BWR) (Ambrosini & Sharabi, 2008). Besides a higher efficiency more focus lies on the safety of a reactor. Power outages, for example caused by natural disasters or technical failure, could lead to failure of circulation pumps. Failure of such active systems, together with other circumstances, could result in a core meltdown. Therefore part of the research is done into nuclear reactors which rely less on pumps to drive the circulation of the coolant. The HPLWR has the potential to overcome this problem by the use of natural convection by placing a riser on top of the core. When the circulation is driven by natural convection pumps are not required to control the circulation and the natural convection provides an extra safety feature during emergencies. Pumps are still in place in case of other control issues, but do not necessarily have to be used to drive the circulation during operation.

The natural convection in the water loop arises as follows. The relatively cold water (280°C) flows from the downcomer into the core where the water is heated up. When the temperature increases from 368°C to 410°C it passes the pseudo-critical temperature (see section 1.2) and the density decreases from around 552 kg/m^3 to around 145 kg/m^3 (see Figure 1.2). So after the fluid has passed the pseudo-critical temperature the density has significantly dropped and the fluid flows from the core into a riser. A riser is placed on top of the core to enhance the process of natural convection. Typically for natural convection driven reactors, such as the existing Economic Simplified Boiling Water Reactor (ESBWR), a riser is set on top of the core. In boiling water reactors natural convection becomes possible due to the phase transition of water from fluid to steam. The density difference between these two phases is used to create a gravitational pressure drop in the system to drive the circulation. A riser is placed on top of the core and a downcomer next to the core to let relative cold water flow downwards. Before the water flows in the downcomer heat is extracted and the water has a higher density. The riser enhances the gravitational pressure drop so that it can support the circulation of the coolant. A comparable density drop is also present in the HPLWR only without a phase transition. In the riser the supercritical water is significantly lighter than the fluid in the downcomer due to the density drop and the resulting pressure drop supports the circulation.

This mechanism also provides a negative feedback loop. Whenever the mass flow rate decreases for some reason the water in the core heats up and reaches the pseudo-critical point earlier in the loop. The density decreases at a lower part of the core and the net force between the downcomer and the core/riser becomes greater, resulting in an increase of the mass flow rate. The exact opposite happens when an increase of the mass flow rate is introduced and the system returns to its steady state eventually.

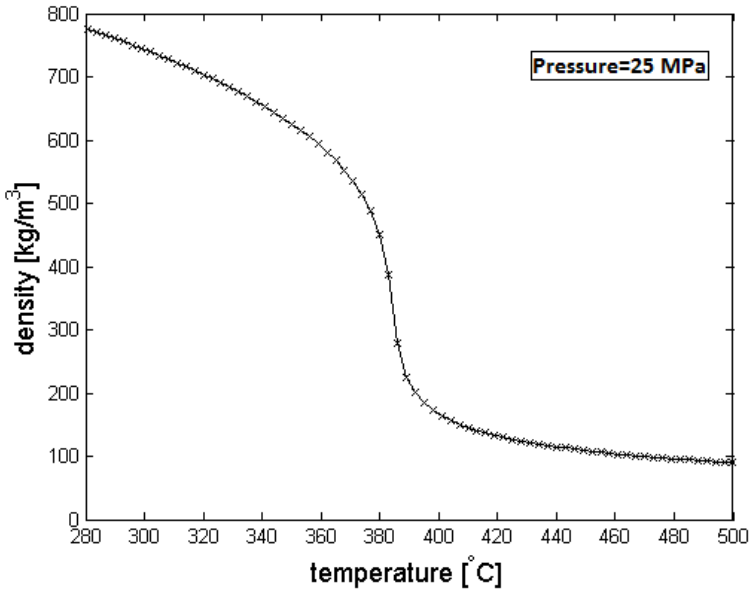

Figure 1.2: Density of water versus temperature at a pressure of 25 MPa. The density drop occurs around the pseudo-critical temperature (384.9°C). Data taken from (NIST, 2011).

1.2 SUPERCRITICAL WATER

Water can exist in four states as shown in Figure 1.3. There exist one state in which the water has gas and fluid like properties, this is called the supercritical state. Water exists in this state when the pressure and the temperature both lie above the critical point of water. This point is located at T_c=373.946°C and p_c=22.0640 MPa. The HPLWR operates under a constant pressure of 25 MPa and therefore the state, liquid or supercritical, of the water depends only on the temperature. As stated earlier, water flows in the core at a temperature of 280°C with the water being in its liquid state. However, as the water heats up in the core it exceeds the critical temperature and becomes supercritical, indicated by the dashed line in Figure 1.3. The HPLWR is considered as an one-phase system, because the lack of a phase transition. A phase transition occurs in a BWR and therefore the BWR is a good example of a two-phase system, because the water is turned into steam in the core.

As the water heats up even more the water passes the pseudo-critical point, which lies at T_{pc}=384.9°C. This pseudo-critical point is defined as the point where the specific heat capacity has its maximum, see Figure 1.4. Water has a highly non-linear behavior around this point. Although there exists no phase change at this point, the density makes a significant drop comparable to the density drop in a BWR due to the phase change. This point is taken as a reference point in this thesis as will be clear in section 2.4. The next table shows a list of properties of water at the pseudo-critical point, which will be used later on.

Table 1.1: Properties of water at the pseudo-critical point. Data taken from (NIST, 2011).

Property	Value
T_{pc}	384.9°C
h_{pc}	$2.1529 \cdot 10^{6}$ J/kg
ρ_{pc}	316.82 kg/m^3
υ_{pc}	$3.1564 \cdot 10^{-3}$ m^3/kg
μ_{pc}	$4.2797 \cdot 10^{-5}$ Pa·s

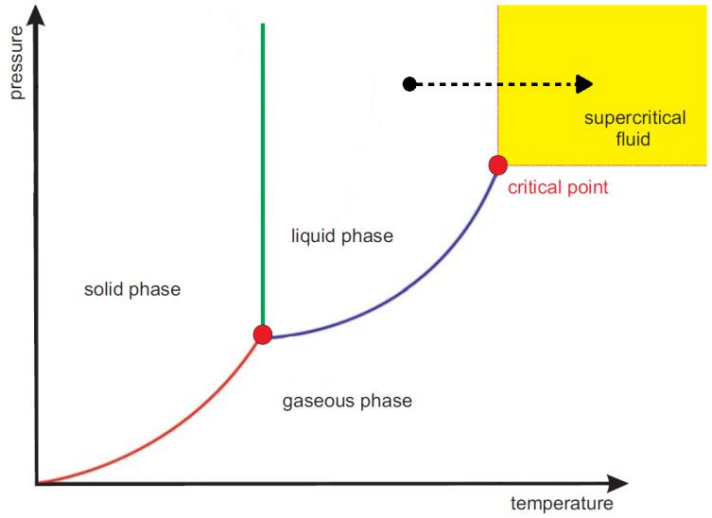

Figure 1.3: Phase diagram of water. As the water heats up in the core the water undergoes a phase change from a liquid state to a supercritical state. Modified image taken from (Ortega Gómez, 2009).

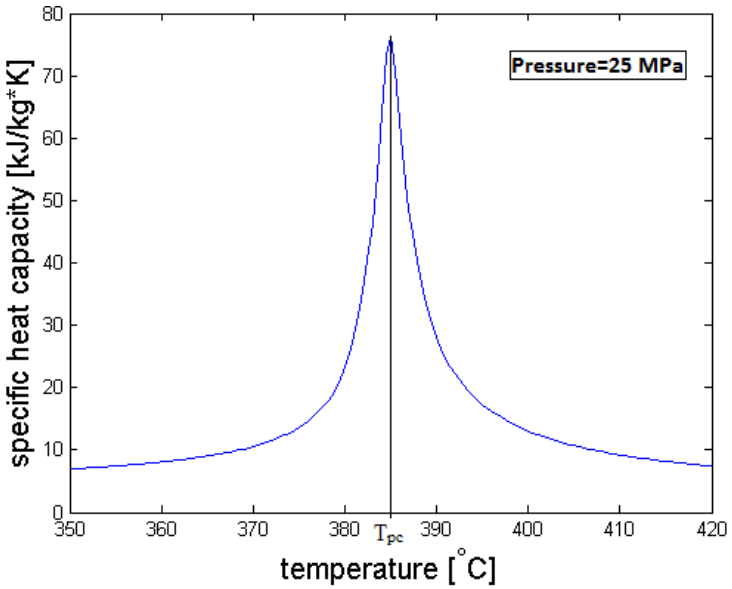

Figure 1.4: Specific heat capacity versus temperature at a pressure of 25 MPa. The pseudo-critical point lies at the maximum of the specific heat capacity. Data taken from (NIST, 2011).

1.3 THE STABILITY PROBLEM

In the last few decades a lot of research has gone into the stability of the water loop in BWRs. In a two-phase flow system, such as the BWR, different type of instabilities were classified by Boure et al. (1973). Density wave oscillations were found to be one the most contributing instabilities present in two-phase flow systems (Papini, Cammin, Colombo, & Ricott, 2012) and are therefore excessively investigated by many through experimental and analytical studies. For instance, Van Bragt (1998) did a research into stability problems associated with natural convection core cooling in BWRs and performed a parametric study to investigate the influence of different parameters on the stability of the water loop. Because in a supercritical water loop a comparable density drop occurs as in a two-phase flow system the presumption arose that density wave oscillation instabilities are also present in these supercritical systems in which only one phase exists. This research investigates the response of a natural circulation driven supercritical water loop to introduced perturbations and checks if similar instabilities as in a BWR are found.

When the system is exposed to a perturbation it can respond in two ways. One possibility is that the perturbation decays over time and the mass flow rate returns to its original state; the steady state mass flow. The second possibility is that the perturbation can grow in time and can make the mass flow to oscillate with increasing amplitude, which is unfavorable. An unstable mass flow can have unwanted consequences. For instance, the water is also used as the moderator and an unstable mass flow could lead to power instability. Also mass flow oscillations could lead to fatigue (or even damage) of reactor components and compromise the safety (Jain & Rizwan-Uddin, 2008). Furthermore, it is possible that the flow rate becomes low enough and that the mass flow becomes unable to cool the core down and reactor components may overheat. It has been shown that the stability of the system depends on various design parameters and operating conditions (Van Bragt, 1998), such as the power, flow rate, inlet temperature and geometry (e.g. the core layout, the axial friction profile and fuel characteristics).

There are different type of instabilities that can occur in a natural circulation driven supercritical water loop. Van Bragt (1998) showed that different type of instabilities were present in a BWR. There are dynamic instabilities which can be solved with a time dependent approach and there are static instabilities which can be solved with the steady state equations. Van Bragt (1998) made a distinction between two types of dynamic instabilities. Type-I instabilities occur with a low frequency and are caused by the gravitational pressure drop. Whereas the Type-II instabilities are of a higher frequency and are caused by frictional pressure drops in the natural circulation loop (Van Bragt, 1998).

Boure et al. (1973) divided the static instabilities into three classes, of which fundamental static instabilities is one of them. Ledinegg instabilities belong to this class of instabilities. A Ledinegg instability is a sudden change of the mass flow to a higher or lower value (Ortega Gómez, 2009). In a water loop driven by a pump these flow changes occur when the pressure versus mass flow rate characteristic of the pump intersects at multiple points with the pressure characteristic of the water loop. An unstable mass flow can then change its mass flow rate abruptly to another mass flow rate, which can be stable. (Ortega Gómez, 2009). However, in this research there is no pump, because the circulation is driven by natural convection. Therefore, another method must be found to search for Ledinegg instabilities.

1.4 LITERATURE SURVEY

Up to now the stability of a supercritical water loop driven by natural convection is not studied as abundantly as flow instabilities in two-phase systems. Also, the HPLWR Phase 2 project focusses its attention mainly on the development of a HPLWR with forced circulation. However, a number of researchers investigated this subject with various approaches. Chatoorgoon (2001) began with investigating the stability of a supercritical water loop driven by natural convection with a non-linear code, called SPORTS, and an analytical model. His analytical model was based on a simplified configuration of a single channel, natural circulation loop with a heat source and sink modeled as a point source. He postulated that the instability boundary for such a system can be approximated with the criterion $\frac{d(flow)}{d(power)} = 0$, instability boundary occurs in the near peak region of the flow versus power characteristic, and found an analytical formulation for the stability boundary. The numerical results from the non-linear code showed good agreement with these analytical results. Chatoorgoon et al. (2005) continued investigating flow instabilities, i.e. parameter study, with the non-linear code SPORTS for different supercritical fluids; H_2O, CO_2 and H_2. Found was that the stability characteristic of supercritical CO_2 was similar to supercritical H_2O, which makes experiments easier to perform due to the fact that CO_2 reaches the supercritical state at a lower pressure and temperature (Chatoorgoon 2005b).

Subsequently, a numerical analysis for flow instabilities of a supercritical loop with CO_2 was performed by Jain and Rizwan-uddin (2008). Non-linear one dimensional equations were set up for a single channel and solved using an implicit finite difference scheme, whereby the water loop was divided into a number of grid points. Neutronic-thermo-hydraulic coupling was not taken into account. The main conclusion of this research was that the instability region is not confined to the peak region of the mass flow rate-power curve (Jain & Rizwan-Uddin, 2008) as opposed to findings by Chatoorgoon et al. (2005b). Results obtained by Sharma et al. (2010) confirmed this conclusion. They performed a steady state and linear stability analysis of a supercritical natural circulation water loop and studied the effect of various design parameters.

Furthermore, Ortega Gómez (2009) investigated the stability of a HPLWR core (forced circulation loop) and did not find Ledinegg instabilities for the operating conditions of a HPLWR. Though, Ambrosini (2011) did an assessment of flow stability boundaries in a heated channel (forced circulation) for different supercritical fluids and found two adjoining regions in the instability domain where Ledinegg instabilities and density wave oscillations occur. Both Ortega Gómez (2009) and Jain (2008) indicated that little to no experimental data was available about the instabilities of a supercritical (forced or natural circulation) water loop at that time. Lomperski et al. (2004) investigated the stability of a supercritical CO_2 natural circulation loop experimentally, but found no flow instabilities and therefore no agreement was found with numerical results obtained by Jain (2008). After their research an experimental setup was built at the Reactor Institute of the TU Delft to investigate the stability of a natural circulation driven supercritical loop experimentally. This setup, named the DeLight ('Delft light water reactor facility'), used Freon R23 as the working fluid for the same reasons CO_2 is used in the research of Jain (2008). Freon R23 has similar properties around the pseudo-critical point as water, only this point is reached at a temperature of 33°C and a pressure of 5.7 MPa (T'Joen & Rohde, 2012).

Neutronic-thermo-hydraulic coupling was taken into account during the experiment and resulted in an instability region for certain operating conditions. Subsequently, Kam (2011) and Spoelstra (2012) worked on numerical modeling of the experimental setup with a computer code. Their results were compared with the experimentally found instability domain, but have matched only partially (Spoelstra, 2012).

1.5 OUTLINE

The impetus for this research was the research done by Guido et al. (1991), which investigated density wave oscillations in parallel boiling water channels with a simplified treatment of the stability problem. They were able to derive explicit expressions for the stability limits of the system by simplifying the model and approaching the stability problem with a linear analysis. A similar approach is applied in this thesis for the stability problem of a natural circulation driven HPLWR. In reality the problem is much more difficult and, therefore, this research deals with the stability problem in a qualitative way. The HPLWR is simplified as much as possible and a linear analysis is done. By simplifying the problem calculations can be done quicker, making parameter studies accessible for instance. Stability maps can be derived rather quick and the stability maps can be investigated extensively for their characteristics. This research performed a parameter study for a natural circulation driven supercritical water loop and a method to find Ledinegg instabilities is proposed. This research is a continuation of the initial work of Rohde, who proposed the simplified water loop model and derived a part of the mathematical foundation presented in this thesis. The next chapter will present the simplification of the HPLWR, will lay down the mathematical foundation for the simplified water loop and prepare the model for a linear analysis. Chapter 3 will continue with the solving of the stability problem followed by chapter 4, which will elaborate on the computational implementation of the stability problem. *Matlab* has been used for the scripting and coding. Chapter 5 will present a parameter study and investigate the type of instabilities occurring in the system. Finally, a conclusion is drawn and thought for discussion and future research is given.

2 MATHEMATICAL FOUNDATION

2.1 THE HIGH PERFORMANCE LIGHT WATER REACTOR

The HPLWR is based on the SCWR concept, see Figure 2.1. The complete design of the HPLWR is presented in the public final report of the HPLWR Phase 2 project (Starflinger, 2010). The aim of this thesis lies on a HPLWR driven by natural convection, but because this concept has not yet been investigated abundantly there are not any schematics of a HPLWR driven by natural convection yet. For that reason the simplified schematic of the SCWR shown in Figure 2.1 does not include a riser and a pump is needed to drive the circulation. Therefore the reader must keep in mind that a riser has to be placed on top of the core to enhance the natural convection.

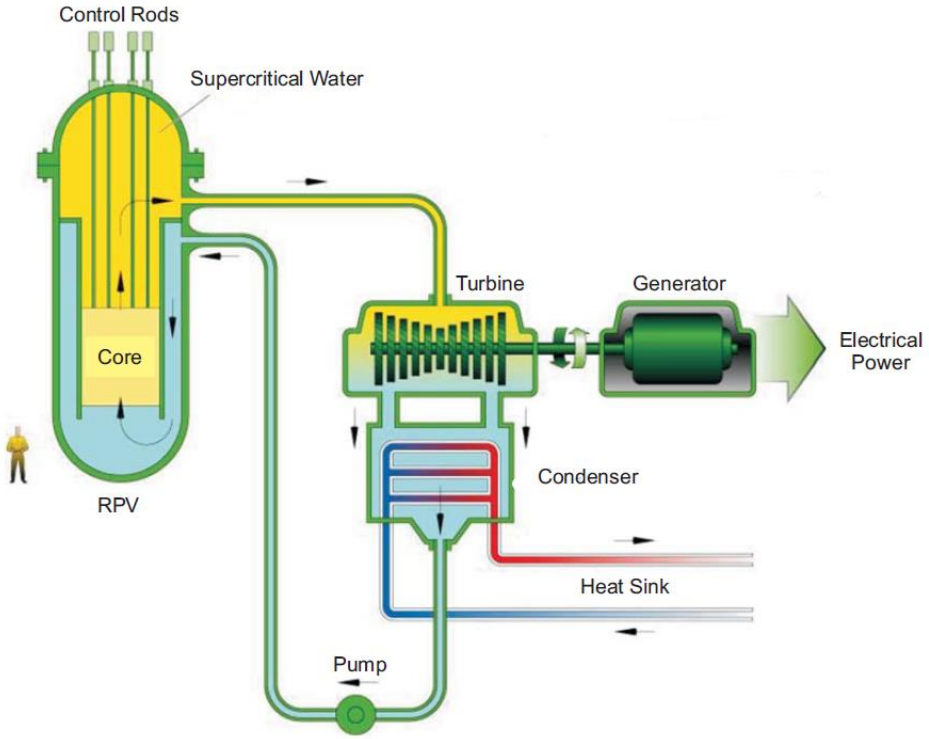

Figure 2.1: A simplified schematic of the SCWR concept. The water heats up in the core and as the volume increases the mass flow rate does as well. The water drives the turbines and the heat is removed with a condenser. Notice that there is no riser present on top of the core and the circulation is not driven by natural convection, but with a pump. Source: (Ortega Gómez, 2009).

The water flows at the bottom of the Reactor Pressure Vessel (RPV) into the core where it undergoes a three stage heating process as shown in Figure 1.1. The inner layout of the RPV is displayed in Figure 2.2a in which the flow of the water is indicated with arrows. The water flows in the upward direction into the evaporator and heats up to a temperature of 390°C and is mixed in the after coming mixing chamber. Then the water flows in the downwards direction through the superheater 1 stage in which it heats up to 433°C. The water is mixed again and then flows upwards into the superheater 2 stage where it finally

leaves the core at a temperature of 500°C. A cross section of the core is displayed in Figure 2.2b. The three stages consist of 52 fuel assembly clusters, which each consists of nine fuel assemblies in which the water flows along the fuel rods. The water passes the pseudo-critical point in the core and has expanded significantly. The water is then led through the riser to create a gravitational pressure drop to drive the natural convection and eventually the water drives the turbines which generate electrical power. After the turbines heat is extracted with a condenser until the water has the desired inlet temperature and then it is led back to the inlet of the core through a annular downcomer surrounding the core. During one cycle the water flows through various channels, bends, mixing chambers and valves. It therefore becomes a complex system when one wants to model the flow of the water.

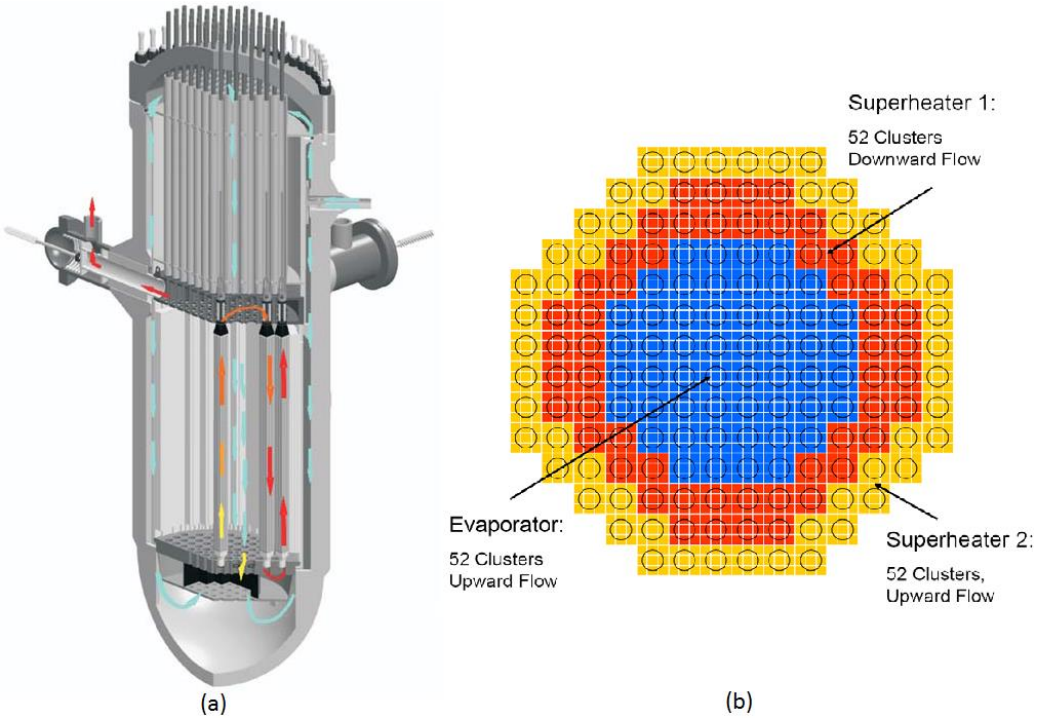

Figure 2.2: (a) Inner layout of the reactor pressure vessel with the direction of the mass flow indicated with arrows. The coolant is led into the core and flows in the upward direction into the evaporator, then downwards in the superheater 1 and finally upwards in the superheater 2 where it leaves the core through one of the hot pipes. Source: (Ortega Gómez, 2009). (b) Cross section of the three-pass core design. Every fuel assembly cluster contains nine fuel assemblies in which the water flows along the fuel rods. Source: (Starflinger, 2010).

Besides the transport of heat from the core the water is also used for the moderation of the neutrons. Fast neutrons collide with the hydrogen atoms of water and lose a part of their kinetic energy. The moderation of the core is therefore dependent on the density in the core. As the water heats up and the density decreases the moderation of the neutrons decreases as well. The power of the core is therefore coupled with the thermo-hydraulic properties of the coolant (Spoelstra, 2012).

Furthermore, as the water heats up in the core it becomes supercritical and as the pseudo-critical temperature is reached various properties of water behave non-linearly, see Figure 2.3. As discussed earlier the density undergoes a sudden drop and the heat capacity has a large peak around the pseudo-

critical temperature. The viscosity also makes a sudden drop in the vicinity of the pseudo-critical temperature and then slowly rises as the temperature increases. This non-linear behavior of the properties play an important role in the heat transfer phenomena in the HPLWR.

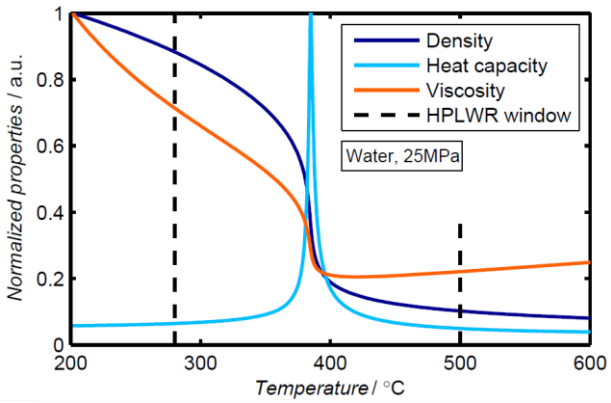

Figure 2.3: Properties of water in the temperature range of the HPLWR. Note that the properties are normalized. Source: (Spoelstra, 2012).

2.2 SIMPLIFICATION OF THE HPLWR

In order to investigate the stability a mathematical foundation for the supercritical water loop must be constructed. The idea is to solve the stability problem with a very simplified approach just as Guido et al. (1991) did for a single boiling water channel. Therefore the HPLWR is simplified as much as possible with a water loop while maintaining the physical properties of the system. The resulting water loop is displayed in section 2.3.

2.2.1 THE EQUATION OF STATE

An important simplification involves the equation of state. The density of water can be written as a function of enthalpy if the pressure is constant, the equation of state. The system should operate under a constant pressure of 25 MPa, but due to gravitational and frictional pressure drops the pressure is not constant throughout the system. Though, the changes of the equation of state due to pressure changes can be neglected and the pressure is assumed to be constant in this thesis. With the use of the equation of state the density and specific volume variables in the upcoming balances can be substituted by the enthalpy. In Figure 2.4 the density and specific volume of water are plotted in red for the specific enthalpy.

In this thesis a two-region approximation for the equation of state is used, indicated by the blue line in Figure 2.4. The density is approximated with a linear function before the pseudo-critical point and the specific volume is approximated with a linear function after the pseudo-critical point. The gradients of the linear functions are C_1=-4.7877·10^{-4} and C_2=0.80·10^{-8} respectively. This gives the following approximation of the equation of state in which υ denotes the specific volume and H the enthalpy.

$$\upsilon_i = \begin{cases} \dfrac{1}{\rho_{pc} + C_1\left(H_i - h_{pc}\right)} & \left(H_i < h_{pc}\right) \\ \upsilon_{pc} + C_2\left(H_i - h_{pc}\right) & \left(H_i \geq h_{pc}\right) \end{cases} \tag{2.1}$$

At the transition between the two different approximations a discontinuity occurs in the slope of the approximation of the equation of state, because the two approximations are set up independently for the two regions. The two approximations of the equation of state intersect at the pseudo-critical point.

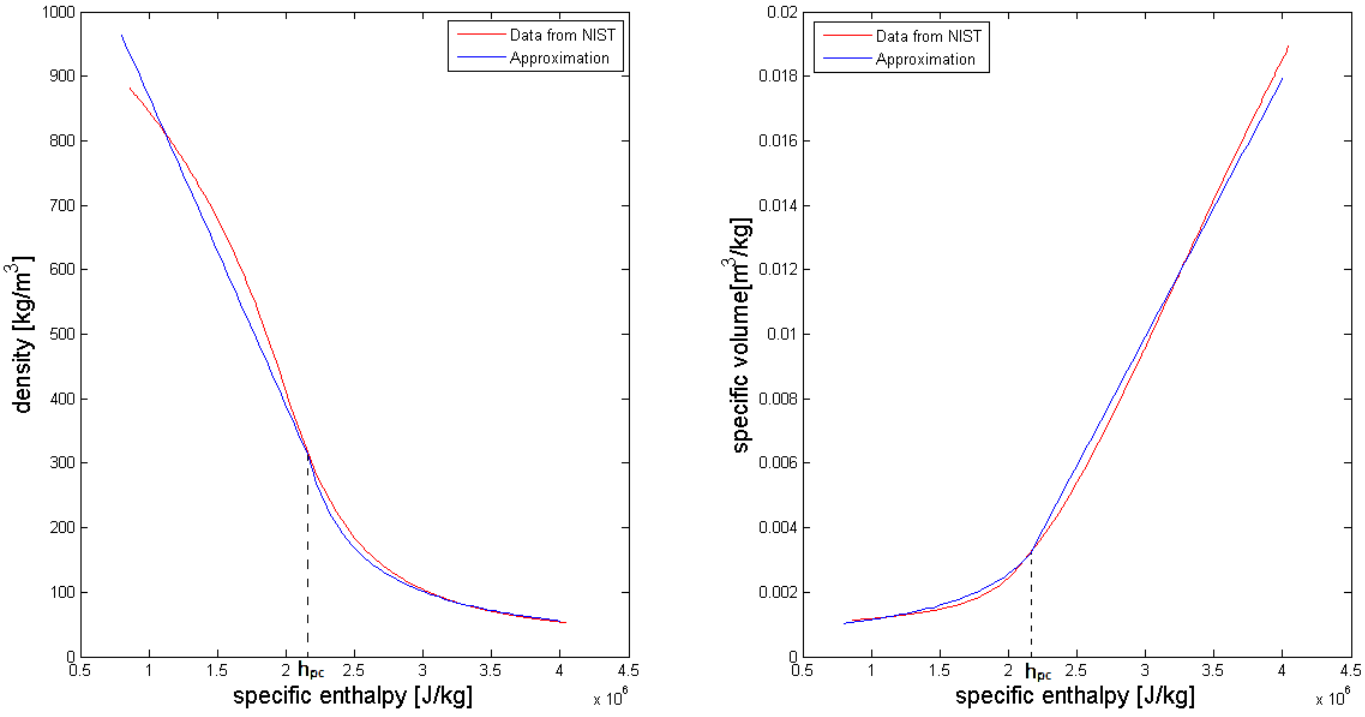

Figure 2.4: The equation of state describes the density as a function of enthalpy. In red the data for water from NIST (2011) and in blue the approximation made in this thesis are plotted. Note the linear behavior of the density before h_{pc} and the linear behavior of the specific volume after h_{pc}.

2.2.2 GEOMETRY

Besides the equation of state further simplifications are made considering the geometry of the HPLWR. The HPLWR is simplified to a 1 dimensional water loop and these simplifications are discussed here.

2.2.2.1 Channel geometry

The core of the HPLWR has many channels through which the water flows along the fuel rods. In this thesis the core is simplified to one single straight channel in which the water flows in the upwards direction and is heated by the inner wall of the channel. A single channel riser is placed directly on top of the core with the same flow area A and hydraulic diameter D_h. These two design parameters are assumed to be constant throughout the whole system. The mixing chambers between the three heating stages in the core are left out of the model.

2.2.2.2 Turbines and heat exchanger

The water in the HPLWR goes through a whole system of turbines and heat exchangers. To simplify this part of the water loop a buffer vessel is introduced after the riser. The buffer vessel allows isobaric expansion of the water and functions as a heat exchanger. In the buffer vessel the water is cooled down to the desired inlet temperature and led to the downcomer. The downcomer in the HPLWR is annular and surrounds the core, but the downcomer is also simplified to a single channel with the same design parameters as the riser and the core.

2.2.2.3 Frictions

The water flow in the HPLWR is subjected to friction of the inner walls of the channels and various restrictions caused by bents, valves and other deformations of the channels. The frictional profile of the entire water loop is therefore highly complex and is simplified in this thesis. The various local restrictions in the channels are modeled with one inlet restriction for each part of the system and the accompanying pressure loss coefficient is denoted with *K.*

Furthermore, the friction due to wall shear is rather complex when the system is composed of many different components and various channels. The system is simplified to a single channel system and therefore the friction caused by the wall shear can be modeled with the Darcy friction factor *f.* Many approximations exist for the Darcy friction factor such as the Haaland equation, Swamee–Jain equation etc. The approximation used in this thesis is the Blasius relation for turbulent flow, discussed further in section 4.2.3. The Reynolds number is present in the Blasius relation and depends inter alia on the dynamic viscosity. As seen in Figure 2.3 the viscosity also displays non-linear behavior, though the dynamic viscosity is set to a constant in this thesis for simplicity. This simplification of the Darcy friction factor results in the same friction factor for each channel.

2.2.2.4 Other simplifications

Besides the basic geometry simplifications a few other aspects of the HPLWR have been simplified. Thermal inertia of the walls is neglected and instant heating of the water by the core is assumed. Also the riser and downcomer are assumed to be isolated and prevent heat losses. The only heat loss present in the system occurs in the buffer vessel where the heat of the water is extracted to simulate the turbines and the heat exchanger in an actual HPLWR.

Moreover, the water acts as the moderator and hence has an influence on the power of the core, especially when the density varies significantly along the height of the core. This neutronic-thermo-hydraulic coupling is not taken into account in this research and the core is assumed to provide a time constant homogeneous heat distribution over the entire length of the core.

2.3 THE WATER LOOP MODEL

The simplifications discussed in the previous section lead to the use of the following simplified water loop models for the HPLWR. There are in fact two different loops that must be considered. As became clear during the research the initial water loop model was insufficient for certain operating conditions. Therefore, two different models had to be set up in order to cover all operating conditions. The first one is based on the fact that the water does not reach the pseudo-critical temperature and the second one applies to the case in which the water reaches the pseudo-critical temperature in the core. The idea behind these models is to qualitatively investigate the instability and to keep the system as simple as possible by dividing it into a few nodes in order to analytically solve for the instability of the system.

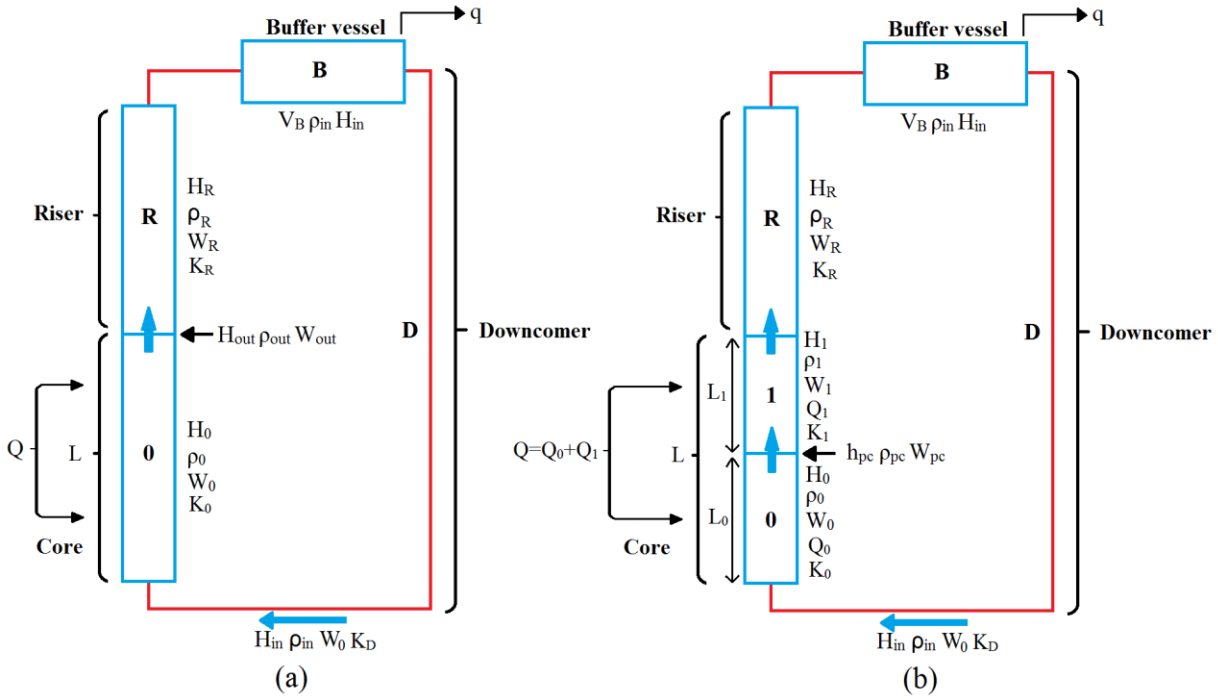

Figure 2.5: (a) The low heating model with four nodes. The enthalpy in the core is assumed to increase linearly and the riser is considered as a perfectly mixed volume. (b) The high heating model with five nodes. The split up of the core is necessary due to the two-region approximation of the equation of state. The riser and node 1 are considered as perfectly mixed volumes.

For the first model the water loop is divided into four nodes, see Figure 2.5a. In this case the power is not large enough to heat the water up till the pseudo-critical point, this can be caused by a low power input or a high mass flow rate. From now on this model will be referred to as the low heating model. The enthalpy of the water in the core is assumed to increase linearly from H_{IN} to H_{out}. An uniform power distribution is applied along the height of the core. The outlet enthalpy H_{out} stays below the pseudo-critical enthalpy and only one approximation is needed for the equation of state. H_{out} is time dependent, because if for instance a perturbation is introduced to the mass flow the outlet enthalpy changes. After the core the water flows into the riser where no heat loss occurs. The riser is considered to be a perfectly mixed volume where the enthalpy is equal to H_1. Besides the core and the riser, there are also the buffer vessel and the downcomer. Because the system should operate under a constant pressure of 25 MPa the

buffer vessel is needed for the isobaric expansion of the heated water. The buffer vessel also acts as the heat exchanger to carry off the heat and to cool the water in the downcomer down to the desired inlet enthalpy H_{IN}. For every node the flow area and the hydraulic diameter is the same and denoted with A and D_h respectively.

For the second model the water loop is divided into five nodes, see Figure 2.5b. This model is based on the situation in which the operating conditions, power and inlet temperature, let the water reach the pseudo-critical point in the core. This model will be referred to as the high heating model. The core is divided into two nodes; indicated with indices 0 and 1. The boundary between these two nodes is defined as the point where the water reaches the pseudo-critical temperature and thus has an enthalpy $h_{pc}=2.15\cdot10^6$ J/kg. The reason for the split up of the core in this model is the approximation of the equation of state. As explained in section 2.2.1 the density and specific volume are approximated with two different linear functions, where the transition from one approximation to the other occurs at the pseudo-critical point. The linearization of these approximations are different for the two approximations and therefore the split up is necessary. The boundary between these two nodes is dynamic, because when for instance the mass flow is increased by a perturbation the pseudo-critical point will be reached later in the core. In node 0 the enthalpy is considered to behave linearly and therefore the enthalpy rises linearly from H_{IN} to h_{pc}. Node 1 of the core as well as the riser are considered as perfectly mixed volumes, where the enthalpy is equal to H_1 and H_R respectively.

2.4 THE LOW HEATING MODEL

This research investigates the stability of the water loop with a linear analysis. Perturbations are introduced to the system and their influence is examined. First the conservation balances are set up for each node of the loop and the number of equations and variables is then reduced. Secondly, the equations are made dimensionless so dimensionless parameters can be derived that are characteristic for the system and stability plots for different setups can be compared. The equations are finally linearized to solve the stability problem with a linear analysis.

2.4.1 CONSERVATION BALANCES

The three different conservation balances are stated here, beginning with the mass balances followed by the energy balances. Finally, the momentum balance is derived and integrated along the entire loop. The subscripts below each variable represent the different nodes in the water loop model. In the equations the time dependent variables are written without the addition of "*(t)*".

2.4.1.1 Mass balances

The low heating model handles the core as one node and, therefore, the length of this node is constant. The enthalpy of the core is assumed to increase linearly from H_{IN} to $H_{out}(t)$. The time dependent outlet enthalpy $H_{out}(t)$ depends on the inlet enthalpy and the power of the core. This makes the density $\rho_0(t)$ of node 0 time dependent as well in contrast with the high heating model, see section 2.5.

$$M_0 : AL\frac{d}{dt}\rho_0 = W_0 - W_{out} \tag{2.2}$$

$$M_R : AL_R\frac{d}{dt}\rho_R = W_{out} - W_R \tag{2.3}$$

$$M_B : \rho_{IN}\frac{d}{dt}V_B = W_R - W_0 \tag{2.4}$$

$$M_D : 0 = W_0 - W_0 = 0 \tag{2.5}$$

W(t) represents the mass flow rate (in kg/s) and $V_B(t)$ is the volume of the buffer vessel. The latter equation equals zero because in the downcomer nothing happens. The density, flow area and length are constant and the flow passes through adiabatically. This equation can therefore be omitted, because it does not contribute to the solution. M_i indicates that the equation follows from the mass balance at node *i*.

Equation (2.6) represents the relation between the density of node 0 and the inlet and outlet density, ρ_{IN} and $\rho_{out}(t)$ respectively. This relation holds, because the density ρ_0(t) is approximated with a linear function of the specific enthalpy before the pseudo-critical point (equation (2.1)) and the enthalpy $H_0(t)$ is assumed to increase linearly. This relation will be substituted in the dimensionless balances.

$$\rho_0 = \tfrac{1}{2}\left(\rho_{IN} + \rho_{out}\right) \tag{2.6}$$

So far there are 3 equations and 6 variables.

Equations:	M_0	M_R	M_B			
Variables:	$\rho_{out}(t)$	$\rho_R(t)$	$V_B(t)$	$W_{out}(t)$	$W_0(t)$	$W_R(t)$

2.4.1.2 Energy balances

Up next are the four energy balances given for each node. The energy balances introduce four extra time dependent variables; $H_R(t)$, $H_0(t)$, $H_{out}(t)$ and $q(t)$. As stated earlier, the enthalpy in node 0 is considered to increase linearly and is time dependent. The inlet enthalpy H_{IN} and the power input *Q* are considered to be the operating conditions and are therefore constant. The energy balances are:

$$E_0 : AL\frac{d}{dt}\rho_0 H_0 = W_0 H_{IN} - W_{out} H_{out} + Q \tag{2.7}$$

$$E_R : AL_R\frac{d}{dt}\rho_R H_R = W_{out} H_{out} - W_R H_R \tag{2.8}$$

$$E_B : \rho_{IN} H_{IN}\frac{d}{dt}V_B = W_R H_R - W_0 H_{IN} - q \tag{2.9}$$

$$E_D : 0 = W_o H_{IN} - W_0 H_{IN} = 0 \tag{2.10}$$

Equation (2.9) can be omitted, because this equation does not determine the solution of the other variables ($V_B(t)$ is not used anywhere). The variable q is then also disregarded. And just as with the mass balance for the downcomer the latter equation E_D can be omitted as well. The enthalpy of node 0 is considered to increase linearly and therefore the enthalpy of node 0 can be written as follows:

$$H_0 = \tfrac{1}{2}\left(H_{IN} + H_{out}\right) \tag{2.11}$$

This relation will also be substituted into the dimensionless balances and leaving in total 5 equations and 8 variables.

Equations:	M_0	M_R	M_B	E_0	E_R			
Variables:	$\rho_{out}(t)$	$\rho_R(t)$	$V_B(t)$	$W_{out}(t)$	$W_0(t)$	$W_R(t)$	$H_{out}(t)$	$H_R(t)$

2.4.1.3 Momentum balance

The momentum balance is integrated along the entire loop. Due to the long derivation only the end result is presented here. The entire derivation for the momentum balance of the high heating model is given in Appendix A. The derivation for the low heating model is analogous.

$$\begin{aligned} &I: AL\frac{d}{dt}W_0 + AL_R\frac{d}{dt}W_R + \frac{d}{dt}V_B W_0 + AL_D\frac{d}{dt}W_0 = \\ &-\frac{1}{2}\left(\frac{f_0 L}{D_h} + K_0\right)\frac{W_0^2}{\rho_0} - \frac{1}{2}\left(\frac{f_R L_R}{D_h} + K_R\right)\frac{W_R^2}{\rho_R} - \frac{1}{2}\left(\frac{f_D L_D}{D_h} + K_D\right)\frac{W_0^2}{\rho_{IN}} \ldots \\ &\ldots - A^2 g\rho_0 L - A^2 g\rho_R L_R + A^2 g\rho_{IN} L_D \end{aligned} \tag{2.12}$$

In this equation f is used for the Darcy friction factor and K represents the pressure loss coefficient due to local changes in the geometry of the system. The line in the middle of equation (2.36) represents the frictional pressure drop due to wall shear and inlet and outlet restrictions and the last line represents the gravitational pressure drop. I denotes the momentum conservation balance.

From the steady state momentum balance the steady state mass flow rate $\bar{W}$ can be calculated and is given below. This quantity will be of use later on when the Froude Number is introduced. In steady state the gravitational pressure drop is equal to the frictional pressure drop, because the gravity drives the circulation and the friction puts a limit on the flow. In the steady state the steady state mass flow rate for each node is equal and can therefore be taken out of the friction term.

$$\bar{W}^2 = gA^2\frac{\rho_{IN}L_D - \bar{\rho}_0 L - \bar{\rho}_R L_R}{\frac{1}{2}\left(\frac{f_0 L}{D_h} + K_0\right)\frac{1}{\bar{\rho}_0} + \frac{1}{2}\left(\frac{f_D L_D}{D_h} + K_D\right)\frac{1}{\rho_{IN}} + \frac{1}{2}\left(\frac{f_R L_R}{D_h} + K_R\right)\frac{1}{\bar{\rho}_R}} \tag{2.13}$$

So in total there are 6 equations and 8 variables.

Equations:	M_0	M_R	M_B	E_0	E_R	I		
Variables:	$\rho_{out}(t)$	$\rho_R(t)$	$V_B(t)$	$W_{out}(t)$	$W_0(t)$	$W_R(t)$	$H_{out}(t)$	$H_R(t)$

2.4.2 REDUCTION OF VARIABLES AND EQUATIONS

The conservation balances for the low heating model are now known. With the use of the mass balance M_R the variable $W_{out}(t)$ can be substituted, because $W_{out}(t)$ has no time derivative. The expression for $W_{out}(t)$ can be written explicitly from equation (2.3):

$$W_{out} = AL_R \frac{d}{dt}\rho_R + W_R \tag{2.14}$$

With this substitution one equation and one variable are omitted. Also the mass balance for the buffer vessel can be substituted into the momentum balance, omitting equation M_B and variable $V_B(t)$. Last but not least, the densities can be substituted with the equation of state and therefore omitting $\rho_{out}(t)$and $\rho_R(t)$. Only 4 equations with 4 variables remain.

Equations:	M_0	E_0	E_R	I
Variables:	$W_0(t)$	$W_R(t)$	$H_{out}(t)$	$H_R(t)$

2.4.3 DIMENSIONLESS BALANCES

So far the balances are set up and the following variables and constants are made dimensionless and inserted into the equations, see Table 2.1. The tildes indicate the dimensionless variables, dimensionless constants and dimensionless equations. The lower characters represent the perturbed variables, which will be present in the linearized equations. Furthermore, $\bar{X}$ denotes the steady state variable.

Table 2.1: These variables and constants are made dimensionless and substituted into the conservation balances.

$\underset{\sim}{\bar{L}}_i \equiv \frac{\bar{L}_i}{L}$	$\underset{\sim}{l}_i \equiv \frac{l_i}{L}$	$\underset{\sim}{t} \equiv \frac{t\bar{W}\upsilon_{pc}}{LA}$
$\underset{\sim}{\bar{W}}_i \equiv \frac{\bar{W}_i}{\bar{W}} = 1$	$\underset{\sim}{w}_i \equiv \frac{w_i}{\bar{W}}$	$\underset{\sim}{h}_i \equiv \frac{h_i\bar{W}}{Q}$
$\underset{\sim}{\bar{H}}_i \equiv \frac{\bar{H}_i\bar{W}}{Q}$	$\underset{\sim}{\rho}_i \equiv \frac{\rho_i}{\rho_{pc}}$	$\underset{\sim}{\bar{\rho}}_i \equiv \frac{\bar{\rho}_i}{\rho_{pc}}$
$\underset{\sim}{\bar{V}}_B \equiv \frac{\bar{V}_B}{AL}$	$\underset{\sim}{D}_h \equiv \frac{D_h}{L}$	

The dimensionless balances are given next. Note that the variables $H_0(t)$, $V_B(t)$ and the densities $\rho_{out}(t)$, $\rho_R(t)$ $\rho_0(t)$ and $\rho_{IN}(t)$ are still present in the dimensionless balances. Substituting these already would reduce the readability and clarity of the equations.

Mass conservation balance

$$\underset{\sim}{M}_0 : \frac{d}{d\underset{\sim}{t}}\underset{\sim}{\rho}_0 = \underset{\sim}{W}_0 - \underset{\sim}{L}_R \frac{d}{d\underset{\sim}{t}}\underset{\sim}{\rho}_R - \underset{\sim}{W}_R \tag{2.15}$$

Energy conservation balances

$$\underset{\sim}{E}_0 : \frac{d}{d\underset{\sim}{t}}\underset{\sim}{\rho}_0\underset{\sim}{H}_0 = \underset{\sim}{W}_0\underset{\sim}{H}_{IN} - \underset{\sim}{H}_{out}\left(\underset{\sim}{L}_R\frac{d}{d\underset{\sim}{t}}\underset{\sim}{\rho}_R + \underset{\sim}{W}_R\right) + 1 \tag{2.16}$$

$$\underset{\sim}{E}_R : \underset{\sim}{L}_R\frac{d}{d\underset{\sim}{t}}\underset{\sim}{\rho}_R\underset{\sim}{H}_R = \underset{\sim}{H}_{out}\left(\underset{\sim}{L}_R\frac{d}{d\underset{\sim}{t}}\underset{\sim}{\rho}_R + \underset{\sim}{W}_R\right) - \underset{\sim}{W}_R\underset{\sim}{H}_R \tag{2.17}$$

Momentum conservation balance

$$\begin{aligned}\underset{\sim}{I} : &\frac{d}{d\underset{\sim}{t}}\underset{\sim}{W}_0 + \underset{\sim}{L}_R\frac{d}{d\underset{\sim}{t}}\underset{\sim}{W}_R + \underset{\sim}{V}_B\frac{d}{d\underset{\sim}{t}}\underset{\sim}{W}_0 + \underset{\sim}{L}_D\frac{d}{d\underset{\sim}{t}}\underset{\sim}{W}_0 = -\underset{\sim}{W}_0\left(\frac{\underset{\sim}{W}_R - \underset{\sim}{W}_0}{\underset{\sim}{\rho}_{IN}}\right)\ldots \\ \ldots &-\frac{1}{2}\left(\frac{f_0}{\underset{\sim}{D}_h} + K_0\right)\frac{\underset{\sim}{W}_0^2}{\underset{\sim}{\rho}_0} - \frac{1}{2}\left(\frac{f_R\underset{\sim}{L}_R}{\underset{\sim}{D}_h} + K_R\right)\frac{\underset{\sim}{W}_R^2}{\underset{\sim}{\rho}_R} - \frac{1}{2}\left(\frac{f_D\underset{\sim}{L}_D}{\underset{\sim}{D}_h} + K_D\right)\frac{\underset{\sim}{W}_0^2}{\underset{\sim}{\rho}_{IN}}\ldots \\ \ldots &-\frac{\underset{\sim}{\rho}_0\underset{\sim}{L}_0}{N_{Fr}} - \frac{\underset{\sim}{\rho}_R\underset{\sim}{L}_R}{N_{Fr}} + \frac{\underset{\sim}{\rho}_{IN}\underset{\sim}{L}_D}{N_{Fr}}\end{aligned} \tag{2.18}$$

The momentum balance has been made dimensionless and the Froude number is substituted for the last three terms, see equation (2.18). The Froude number is a dimensionless quantity that represents the influence of the gravity with respect to convection. The steady state mass flow rate $\bar{W}$ can be calculated with equation (2.13), because it needs to be substituted in the Froude number.

$$N_{Fr} = \frac{\bar{W}^2\upsilon_{pc}^2}{gLA^2} \tag{2.19}$$

2.4.4 LINEARIZED CONSERVATION BALANCES

In this research the problem is solved with a linear approach and will be explained in chapter 3. In order to investigate the stability with linear analysis the dimensionless balances have to be linearized. The variables are substituted with the steady state solution and a perturbation, indicated with a lowercase character: $\underset{\sim}{X} = \underset{\sim}{\bar{X}} + \underset{\sim}{x}$. The assumption is made that the perturbations are very small and multiplications of perturbations are even smaller and are therefore neglected. For example:

$$\underset{\sim}{X}_i \cdot \underset{\sim}{X}_j = \left(\underset{\sim}{\bar{X}}_i + \underset{\sim}{x}_i\right)\left(\underset{\sim}{\bar{X}}_j + \underset{\sim}{x}_i\right) = \underset{\sim}{\bar{X}}_i\underset{\sim}{\bar{X}}_j + \underset{\sim}{\bar{X}}_i\underset{\sim}{x}_j + \underset{\sim}{x}_i\underset{\sim}{\bar{X}}_j + \cancel{\underset{\sim}{x}_i\underset{\sim}{x}_i}$$

Also during the linearization the terms $\underset{\sim}{x}_i\frac{d}{d\underset{\sim}{t}}\underset{\sim}{x}_j$ are assumed to be very small and neglected. When the equations are linearized, the steady state balances are subtracted from the linearized equations in order to investigate the solution of the stability problem around the steady state.

To eliminate the specific volumes $\upsilon_0=1/\rho_0$ and $\upsilon_R=1/\rho_R$ in the linearized momentum balance the approximation of the equation of state has to be linearized as well. In the low heating model the water stays below the pseudo-critical point and therefore $\upsilon_0(t)$ and $\upsilon_R(t)$ always lie below the specific volume υ_{pc} at the pseudo-critical point. Therefore only the first part of equation (2.1) has to be linearized for now. This can be done with a Taylor expansion (see Appendix A) where the higher order terms can be neglected, because these are multiplications of perturbations and therefore very small.

$$\upsilon_i \equiv \frac{1}{\rho_i} = \frac{1}{\rho_{pc} + C_1\left(H_i - h_{pc}\right)} = \frac{1}{\rho_{pc} + C_1\left(\bar{H}_i + h_i - h_{pc}\right)} \approx \frac{1}{\rho_{pc} + C_1\left(\bar{H}_i - h_{pc}\right)} + \frac{-C_1}{\left[\rho_{pc} + C_1\left(\bar{H}_i - h_{pc}\right)\right]^2} h_i + \ldots \tag{2.20}$$

The linearization of the perturbed variable follows from this Taylor expansion (indicated with red in equation (2.20)) and is stated in equation (2.21) in its dimensionless form. Due to the limited symbols, the notation $\breve{\upsilon}_i$ is used here for the indication of the perturbed variable for the specific volume. Furthermore, the linearization of ρ_i is simpler and its dimensionless perturbed variable is given in equation (2.22).

$$\breve{\upsilon}_i = \frac{-C_1 N_{\Delta h} h_{pc} \upsilon_{pc}}{\bar{\rho}_i^{\,2}} \breve{h}_i \tag{2.21}$$

$$\breve{\rho}_i = C_1 N_{\Delta h} h_{pc} \upsilon_{pc} \breve{h}_i \tag{2.22}$$

$N_{\Delta h}$ is a dimensionless parameter that is a measure for the operating conditions of the setup. This parameter is explained further in chapter 3. For now the definition will suffice.

$$N_{\Delta h} = \frac{Q}{\bar{W} h_{pc}} \tag{2.23}$$

2.4.4.1 Linearized mass balances

First, the mass balance is linearized. The density of node 0 is taken as the mean of the inlet density and the outlet density, see equation (2.6). The inlet density is constant and the outlet density can vary, which means that the perturbation of the density at node 0 can be written as follows: $\breve{\rho}_0 = \frac{1}{2}\breve{\rho}_{out}$. The expression is used in the mass and energy balances to substitute the variable $\breve{\rho}_0$. At the same time the perturbed variable for the density is substituted with equation (2.22).

$$\breve{M}_0 : C_1 N_{\Delta h} h_{pc} v_{pc} \left(\tfrac{1}{2} \frac{d}{d\breve{t}} \breve{h}_{out} + \breve{L}_R \frac{d}{d\breve{t}} \breve{h}_R \right) = \breve{w}_0 - \breve{w}_R \tag{2.24}$$

2.4.4.2 Linearized energy balances

The energy balances are linearized next. Remember that the steady state solutions, where the time derivatives are set to zero, are subtracted from the linearized equations. The perturbed variable of the enthalpy can be written down in the same manner as the density $\underset{\sim}{\rho}_0$; $\underset{\sim}{h}_0 = \frac{1}{2}\underset{\sim}{h}_{out}$. The perturbed variable for the density is again substituted, see equation (2.22).

$$\underset{\sim}{E}_0 : \left(\tfrac{1}{2}\bar{\underset{\sim}{\rho}}_0 + \tfrac{1}{2}C_1 N_{\Delta h} h_{pc} v_{pc} \bar{\underset{\sim}{H}}_0\right)\frac{d}{d\underset{\sim}{t}}\underset{\sim}{h}_{out} + C_1 N_{\Delta h} h_{pc} v_{pc} \bar{\underset{\sim}{H}}_{out} \underset{\sim}{L}_R \frac{d}{d\underset{\sim}{t}}\underset{\sim}{h}_R = -\underset{\sim}{h}_{out} - \underset{\sim}{w}_R \bar{\underset{\sim}{H}}_{out} + \underset{\sim}{w}_0 \underset{\sim}{H}_{IN} \quad (2.25)$$

$$\underset{\sim}{E}_R : \left(\underset{\sim}{L}_R \bar{\underset{\sim}{\rho}}_R + \underset{\sim}{L}_R C_1 N_{\Delta h} h_{pc} v_{pc}\left(\bar{\underset{\sim}{H}}_R - \bar{\underset{\sim}{H}}_{out}\right)\right)\frac{d}{d\underset{\sim}{t}}\underset{\sim}{h}_R = \underset{\sim}{h}_{out} + \bar{\underset{\sim}{H}}_{out}\underset{\sim}{w}_R - \underset{\sim}{h}_R - \underset{\sim}{w}_R \bar{\underset{\sim}{H}}_R \quad (2.26)$$

2.4.4.3 Linearized momentum balance

The momentum balance is linearized and substituted with equations (2.21) and (2.22). The steady state variable $\bar{\underset{\sim}{V}}_B$ is still present, but is independent of time and determined from outside the model.

$$\begin{aligned}
&\underset{\sim}{I} : \left(1 + \underset{\sim}{L}_D + \bar{\underset{\sim}{V}}_B\right)\frac{d}{d\underset{\sim}{t}}\underset{\sim}{w}_0 + \underset{\sim}{L}_R \frac{d}{d\underset{\sim}{t}}\underset{\sim}{w}_R = -\left(\left(\frac{f_R \underset{\sim}{L}_R}{\underset{\sim}{D}_h} + K_R\right)\bar{\underset{\sim}{\upsilon}}_R + \underset{\sim}{\upsilon}_{IN}\right)\underset{\sim}{w}_R + \ldots \\
&\ldots \tfrac{1}{2}\left(\tfrac{1}{2}\left(\frac{f_0}{\underset{\sim}{D}_h} + K_0\right)\frac{1}{\bar{\underset{\sim}{\rho}}_0^{\,2}} - \frac{1}{N_{Fr}}\right)C_1 N_{\Delta h} h_{pc} v_{pc} h_{out} + \left(\tfrac{1}{2}\left(\frac{f_R \underset{\sim}{L}_R}{\underset{\sim}{D}_h} + K_R\right)\frac{1}{\bar{\underset{\sim}{\rho}}_R^{\,2}} - \frac{\underset{\sim}{L}_R}{N_{Fr}}\right)C_1 N_{\Delta h} h_{pc} v_{pc} \underset{\sim}{h}_R + \ldots \\
&\ldots \left(\underset{\sim}{\upsilon}_{IN} - \left(\frac{f_0}{\underset{\sim}{D}_h} + K_0\right)\bar{\underset{\sim}{\upsilon}}_0 - \left(\frac{f_D \underset{\sim}{L}_D}{\underset{\sim}{D}_h} + K_D\right)\underset{\sim}{\upsilon}_{IN}\right)\underset{\sim}{w}_0
\end{aligned} \quad (2.27)$$

In total there are now 4 dimensionless equations with 4 dimensionless perturbed variables to investigate.

Equations:	$\underset{\sim}{M}_0$	$\underset{\sim}{E}_0$	$\underset{\sim}{E}_R$	$\underset{\sim}{I}$
Variables:	$\underset{\sim}{w}_0(t)$	$\underset{\sim}{w}_R(t)$	$\underset{\sim}{h}_{out}(t)$	$\underset{\sim}{h}_R(t)$

2.5 THE HIGH HEATING MODEL

In the high heating model the water reaches the pseudo-critical point in the core and therefore the core is split up into two nodes. The construction of the mathematical foundation for this water loop is analogous to the low heating model and, therefore, this section handles the derivation of the conservation balances a bit more concise.

2.5.1 CONSERVATION BALANCES

Again, the mass, energy and momentum balances are set up for each node first. Balances that do not contribute to the stability problem will be omitted in advance.

2.5.1.1 Mass balances

The following four mass balances can be set for four nodes of the loop, mass balance M_D is omitted. Remember that the length $L_0(t)$ and $L_1(t)$ are variable due to the dynamic boundary in the core where the water reaches h_{pc}, and therefore they are inside the time derivative. L is used for the total length of the core.

Furthermore, the enthalpy H_0 is constant in contrast with the low heating model. The enthalpy is assumed to increase linearly from H_{IN} to h_{pc} in node 0 and therefore H_0 can be written with equation (2.28). The density ρ_0 is therefore also constant and can be calculated with equation (2.1).

$$H_0 = \tfrac{1}{2}\left(H_{IN} + h_{pc}\right) \tag{2.28}$$

$$M_0 : A\rho_0 \frac{d}{dt} L_0 = W_0 - W_{pc} \tag{2.29}$$

$$M_1 : A\frac{d}{dt} \rho_1 L_1 = W_{pc} - W_1 \tag{2.30}$$

$$M_R : AL_R \frac{d}{dt} \rho_R = W_1 - W_R \tag{2.31}$$

$$M_B : \rho_{IN} \frac{d}{dt} V_B = W_R - W_0 \tag{2.32}$$

There are now 4 equations and 9 variables.

Equations:	M_0	M_1	M_R	M_B					
Variables:	$\rho_1(t)$	$\rho_R(t)$	$V_B(t)$	$W_1(t)$	$W_{pc}(t)$	$W_0(t)$	$W_R(t)$	$L_0(t)$	$L_1(t)$

2.5.1.2 Energy balances

Up next are the three energy balances given for the nodes, energy balances E_D and E_B are omitted for the same reasoning as with the low heating model. The energy balances introduce two more variables; $H_1(t)$ and $H_R(t)$. As stated earlier, the enthalpy in node 0 is considered to increase linearly and is constant. The energy balances are:

$$E_0 : A\rho_0 H_0 \frac{d}{dt} L_0 = W_0 H_{IN} - W_{pc} h_{pc} + Q \frac{L_0}{L} \tag{2.33}$$

$$E_1 : A \frac{d}{dt} \rho_1 L_1 H_1 = W_{pc} h_{pc} - W_1 H_1 + Q \frac{L_1}{L} \tag{2.34}$$

$$E_R : A L_R \frac{d}{dt} \rho_R H_R = W_1 H_1 - W_R H_R \tag{2.35}$$

The power is uniformly distributed over the entire length of the core and therefore the power is distributed with the same ratio as for the heated lengths of each node. So far there are 7 equations and 11 variables.

Equations:	M_0	M_1	M_R	M_B	E_0	E_1	E_R				
Variables:	$\rho_1(t)$	$\rho_R(t)$	$V_B(t)$	$W_1(t)$	$W_{pc}(t)$	$W_0(t)$	$W_R(t)$	$L_0(t)$	$L_1(t)$	$H_1(t)$	$H_R(t)$

2.5.1.3 Momentum balance

The momentum balance is again integrated along the entire loop. For the entire derivation, see Appendix A.

$$\begin{aligned} I : & A\frac{d}{dt} W_0 L_0 + A\frac{d}{dt} W_1 L_1 + AL_R \frac{d}{dt} W_R + \frac{d}{dt} V_B W_0 + AL_D \frac{d}{dt} W_0 = \\ & -\frac{1}{2}\left(\frac{f_0 L_0}{D_h} + K_0 \right) \frac{W_0^2}{\rho_0} - \frac{1}{2}\left(\frac{f_1 L_1}{D_h} + K_1 \right) \frac{W_1^2}{\rho_1} - \frac{1}{2}\left(\frac{f_R L_R}{D_h} + K_R \right) \frac{W_R^2}{\rho_R} - \frac{1}{2}\left(\frac{f_D L_D}{D_h} + K_D \right) \frac{W_0^2}{\rho_{IN}} \ldots \\ & \ldots - A^2 g \rho_0 L_0 - A^2 g \rho_1 L_1 - A^2 g \rho_R L_R + A^2 g \rho_{IN} L_D \end{aligned} \tag{2.36}$$

The steady state mass flow rate for the high heating model is stated below.

$$\bar{W}^2 = gA^2 \frac{\rho_{IN} L_D - \rho_0 \bar{L}_0 - \bar{\rho}_1 \left(\bar{L}_1 + L_R \right)}{\frac{1}{2}\left(\frac{f_0 \bar{L}_0}{D_h} + K_0 \right) \frac{1}{\rho_0} + \frac{1}{2}\left(\frac{f_D L_D}{D_h} + K_D \right) \frac{1}{\rho_{IN}} + \frac{1}{2}\left(\frac{f_1 \bar{L}_1}{D_h} + K_1 + \frac{f_R L_R}{D_h} + K_R \right) \frac{1}{\bar{\rho}_1}} \tag{2.37}$$

The momentum balance adds one equation to the number of equations.

Equations:	M_0	M_1	M_R	M_B	E_0	E_1	E_R	I			
Variables:	$\rho_1(t)$	$\rho_R(t)$	$V_B(t)$	$W_1(t)$	$W_{pc}(t)$	$W_0(t)$	$W_R(t)$	$L_0(t)$	$L_1(t)$	$H_1(t)$	$H_R(t)$

2.5.2 *REDUCTION OF VARIABLES AND EQUATIONS*

With the use of the following equations the number of variables and equations can be reduced.

$$L_0 = L - L_1 \tag{2.38}$$

$$W_{pc} = W_0 \frac{H_{IN}}{h_{pc}} + \frac{Q}{h_{pc}} \frac{L_0}{L} - A\rho_0 \frac{H_0}{h_{pc}} \frac{d}{dt} L_0 \tag{2.39}$$

The first equation also implies that $\frac{d}{dt} L_0 = -\frac{d}{dt} L_1$. The latter equation is a result of equation (2.33). We may express W_{pc} in the other variables, because W_{pc} has no time derivative in any of the balances. This eliminates one equation and one variable. Furthermore, the densities are substituted with the approximation of the equation of state (equation (2.1)). The mass balance M_B is also substituted in the momentum balance just as with the low heating model, omitting $V_B(t)$ and M_B. Then 6 equations and 6 variables remain.

Equations:	M_0	M_1	M_R	E_1	E_R	I
Variables:	$L_1(t)$	$H_1(t)$	$H_R(t)$	$W_1(t)$	$W_0(t)$	$W_R(t)$

2.5.3 *DIMENSIONLESS BALANCES*

Subsequently, the equations are made dimensionless with the dimensionless variables and constants defined in Table 2.1. The densities and the volume of the buffer vessel are not substituted yet in the dimensionless balances for the sake of clarity.

Mass conservation balances

$$\underset{\sim}{M}_0 : \underset{\sim}{\rho}_0 \left(\frac{\underset{\sim}{H}_0}{\underset{\sim}{h}_{pc}} - 1 \right) \frac{d}{d\underset{\sim}{t}} \underset{\sim}{L}_1 = \left(1 - \frac{\underset{\sim}{H}_{IN}}{\underset{\sim}{h}_{pc}} \right) \underset{\sim}{W}_0 - \frac{1}{\underset{\sim}{h}_{pc}} (1 - \underset{\sim}{L}_1) \tag{2.40}$$

$$\underset{\sim}{M}_1 : \left(\underset{\sim}{\rho}_1 - \frac{\underset{\sim}{H}_0}{\underset{\sim}{h}_{pc}} \underset{\sim}{\rho}_0 \right) \frac{d}{d\underset{\sim}{t}} \underset{\sim}{L}_1 + \underset{\sim}{L}_1 \frac{d}{d\underset{\sim}{t}} \underset{\sim}{\rho}_1 = \frac{\underset{\sim}{H}_{IN}}{\underset{\sim}{h}_{pc}} \underset{\sim}{W}_0 + \frac{1}{\underset{\sim}{h}_{pc}} (1 - \underset{\sim}{L}_1) - \underset{\sim}{W}_1 \tag{2.41}$$

$$\underset{\sim}{M}_R : \underset{\sim}{L}_R \frac{d}{d\underset{\sim}{t}} \underset{\sim}{\rho}_R = \underset{\sim}{W}_1 - \underset{\sim}{W}_R \tag{2.42}$$

Energy conservation balances

$$\underset{\sim}{E}_1 : \left(\underset{\sim}{\rho}_1 \underset{\sim}{H}_1 - \underset{\sim}{H}_0 \underset{\sim}{\rho}_0 \right) \frac{d}{d\underset{\sim}{t}} \underset{\sim}{L}_1 + \underset{\sim}{L}_1 \frac{d}{d\underset{\sim}{t}} \underset{\sim}{\rho}_1 \underset{\sim}{H}_1 = \underset{\sim}{H}_{IN} \underset{\sim}{W}_0 - \underset{\sim}{W}_1 \underset{\sim}{H}_1 + 1 \tag{2.43}$$

$$\underset{\sim}{E}_R : \underset{\sim}{L}_R \frac{d}{d\underset{\sim}{t}} \underset{\sim}{\rho}_R \underset{\sim}{H}_R = \underset{\sim}{W}_1 \underset{\sim}{H}_1 - \underset{\sim}{W}_R \underset{\sim}{H}_R \tag{2.44}$$

Momentum conservation balance

$$\underset{\sim}{I}: -\underset{\sim}{W}_0 \frac{d}{d\underset{\sim}{t}}\underset{\sim}{L}_1 + \left(1-\underset{\sim}{L}_1\right)\frac{d}{d\underset{\sim}{t}}\underset{\sim}{W}_0 + \frac{d}{d\underset{\sim}{t}}\underset{\sim}{W}_1\underset{\sim}{L}_1 + \underset{\sim}{L}_R\frac{d}{d\underset{\sim}{t}}\underset{\sim}{W}_R + \underset{\sim}{V}_B\frac{d}{d\underset{\sim}{t}}\underset{\sim}{W}_0 + \underset{\sim}{L}_D\frac{d}{d\underset{\sim}{t}}\underset{\sim}{W}_0 = -\underset{\sim}{W}_0\left(\frac{\underset{\sim}{W}_R - \underset{\sim}{W}_0}{\underset{\sim}{\rho}_{IN}}\right)\ldots$$
$$\ldots -\frac{1}{2}\left(\frac{f_0\underset{\sim}{L}_0}{\underset{\sim}{D}_h} + K_0\right)\frac{\underset{\sim}{W}_0^2}{\underset{\sim}{\rho}_0} - \frac{1}{2}\left(\frac{f_1\underset{\sim}{L}_1}{\underset{\sim}{D}_h} + K_1\right)\frac{\underset{\sim}{W}_1^2}{\underset{\sim}{\rho}_1} - \frac{1}{2}\left(\frac{f_R\underset{\sim}{L}_R}{\underset{\sim}{D}_h} + K_R\right)\frac{\underset{\sim}{W}_R^2}{\underset{\sim}{\rho}_R} - \frac{1}{2}\left(\frac{f_D\underset{\sim}{L}_D}{\underset{\sim}{D}_h} + K_D\right)\frac{\underset{\sim}{W}_0^2}{\underset{\sim}{\rho}_{IN}}\ldots \qquad (2.45)$$
$$\ldots -\frac{\underset{\sim}{\rho}_0\underset{\sim}{L}_0}{N_{Fr}} - \frac{\underset{\sim}{\rho}_1\underset{\sim}{L}_1}{N_{Fr}} - \frac{\underset{\sim}{\rho}_R\underset{\sim}{L}_R}{N_{Fr}} + \frac{\underset{\sim}{\rho}_{IN}\underset{\sim}{L}_D}{N_{Fr}}$$

2.5.4 LINEARIZED CONSERVATION BALANCES

In the high heating model the water in node 1 of the core has passed the pseudo-critical point and therefore the second approximation of the equation of state applies. This one has to be linearized as well for the perturbed variables $\breve{\underset{\sim}{\rho}}_i$ and $\breve{\underset{\sim}{\upsilon}}_i$. This is done in the same manner as in section 2.4.4 with a Taylor expansion for $\breve{\underset{\sim}{\rho}}_i$. The perturbed variables are presented below in their dimensionless form.

$$\breve{\underset{\sim}{\rho}}_i = \frac{-C_2 N_{\Delta h} h_{pc}}{\upsilon_{pc}\bar{\underset{\sim}{\upsilon}}_i^2}\underset{\sim}{h}_i \qquad (2.46)$$

$$\breve{\underset{\sim}{\upsilon}}_i = \frac{C_2 N_{\Delta h} h_{pc}}{\upsilon_{pc}}\underset{\sim}{h}_i \qquad (2.47)$$

2.5.4.1 Linearized mass balances

The three dimensionless mass balances have been linearized and equation (2.46) is substituted in the equations when necessary. Remember that the steady state solutions are subtracted from the equations in order to investigate the stability problem around steady state conditions.

$$\underset{\sim}{M}_0: \underset{\sim}{\rho}_0\left(\frac{\underset{\sim}{H}_0}{\underset{\sim}{h}_{pc}} - 1\right)\frac{d}{d\underset{\sim}{t}}\underset{\sim}{l}_1 = \left(1 - \frac{\underset{\sim}{H}_{IN}}{\underset{\sim}{h}_{pc}}\right)\underset{\sim}{w}_0 + \frac{1}{\underset{\sim}{h}_{pc}}\underset{\sim}{l}_1 \qquad (2.48)$$

$$\underset{\sim}{M}_1: \left(\frac{1}{\bar{\underset{\sim}{\upsilon}}_1} - \frac{\underset{\sim}{H}_0}{\underset{\sim}{h}_{pc}}\underset{\sim}{\rho}_0\right)\frac{d}{d\underset{\sim}{t}}\underset{\sim}{l}_1 - \frac{\bar{\underset{\sim}{L}}_1 N_{\Delta h} C_1 h_{pc}}{\upsilon_{pc}\bar{\underset{\sim}{\upsilon}}_1^2}\frac{d}{d\underset{\sim}{t}}\underset{\sim}{h}_1 = \frac{\underset{\sim}{H}_{IN}}{\underset{\sim}{h}_{pc}}\underset{\sim}{w}_0 - \frac{1}{\underset{\sim}{h}_{pc}}\underset{\sim}{l}_1 - \underset{\sim}{w}_1 \qquad (2.49)$$

$$\underset{\sim}{M}_R: -\frac{\underset{\sim}{L}_R N_{\Delta h} C_1 h_{pc}}{\upsilon_{pc}\bar{\underset{\sim}{\upsilon}}_R^2}\frac{d}{d\underset{\sim}{t}}\underset{\sim}{h}_R = \underset{\sim}{w}_1 - \underset{\sim}{w}_R \qquad (2.50)$$

2.5.4.2 Linearized energy balances

The energy balances are linearized next. Once again, the perturbed variables for the densities and the specific volumes have been substituted.

$$\underset{\sim}{E}_1 : \left(\frac{\bar{\underset{\sim}{H}}_1}{\bar{\underset{\sim}{\upsilon}}_1} - \underset{\sim}{H}_0 \underset{\sim}{\rho}_0 \right) \frac{d}{d\underset{\sim}{t}} \underset{\sim}{l}_1 + \frac{\bar{\underset{\sim}{L}}_1}{\bar{\underset{\sim}{\upsilon}}_1} \left(1 - \frac{N_{\Delta h} C_1 h_{pc} \bar{\underset{\sim}{H}}_1}{\upsilon_{pc} \bar{\underset{\sim}{\upsilon}}_1} \right) \frac{d}{d\underset{\sim}{t}} \underset{\sim}{h}_1 = \underset{\sim}{H}_{IN} \underset{\sim}{w}_0 - \underset{\sim}{h}_1 - \underset{\sim}{w}_1 \bar{\underset{\sim}{H}}_1 \tag{2.51}$$

$$\underset{\sim}{E}_R : \frac{\bar{\underset{\sim}{L}}_R}{\bar{\underset{\sim}{\upsilon}}_R} \left(1 - \frac{N_{\Delta h} C_1 h_{pc} \bar{\underset{\sim}{H}}_R}{\upsilon_{pc} \bar{\underset{\sim}{\upsilon}}_R} \right) \frac{d}{d\underset{\sim}{t}} \underset{\sim}{h}_R = \underset{\sim}{h}_1 + \underset{\sim}{w}_1 \bar{\underset{\sim}{H}}_1 - \underset{\sim}{h}_R - \underset{\sim}{w}_R \bar{\underset{\sim}{H}}_R \tag{2.52}$$

2.5.4.3 Linearized momentum balance

Finally, the momentum balance is linearized.

$$\begin{aligned}
&\underset{\sim}{I} : \left(1 - \bar{\underset{\sim}{L}}_1 + \underset{\sim}{L}_D + \bar{\underset{\sim}{V}}_B \right) \frac{d}{d\underset{\sim}{t}} \underset{\sim}{w}_0 + \bar{\underset{\sim}{L}}_1 \frac{d}{d\underset{\sim}{t}} \underset{\sim}{w}_1 + \underset{\sim}{L}_R \frac{d}{d\underset{\sim}{t}} \underset{\sim}{w}_R = \\
&\left(\frac{1}{2} \left(\frac{f_0 \underset{\sim}{\upsilon}_0}{\underset{\sim}{D}_h} - \frac{f_1 \bar{\underset{\sim}{\upsilon}}_1}{\underset{\sim}{D}_h} \right) + \frac{1}{\underset{\sim}{\upsilon}_0 N_{Fr}} - \frac{1}{N_{Fr} \bar{\underset{\sim}{\upsilon}}_1} \right) \underset{\sim}{l}_1 - \left(\left(\frac{f_0 \bar{\underset{\sim}{L}}_0}{\underset{\sim}{D}_h} + K_0 \right) \underset{\sim}{\upsilon}_0 + \left(\frac{f_D \underset{\sim}{L}_D}{\underset{\sim}{D}_h} + K_D \right) \underset{\sim}{\upsilon}_{IN} - \underset{\sim}{\upsilon}_{IN} \right) \underset{\sim}{w}_0 \ldots \\
&\ldots - \left(\frac{f_1 \bar{\underset{\sim}{L}}_1}{\underset{\sim}{D}_h} + K_1 \right) \bar{\underset{\sim}{\upsilon}}_1 \underset{\sim}{w}_1 + \left(-\frac{1}{2} \left(\frac{f_1 \bar{\underset{\sim}{L}}_1}{\underset{\sim}{D}_h} + K_1 \right) + \frac{\bar{\underset{\sim}{L}}_1}{\bar{\underset{\sim}{\upsilon}}_1^{\,2} N_{Fr}} \right) \frac{N_{\Delta h} C_1 h_{pc}}{\upsilon_{pc}} \underset{\sim}{h}_1 \ldots \\
&\ldots - \left(\frac{f_R \underset{\sim}{L}_R}{\underset{\sim}{D}_h} + K_R + \frac{\underset{\sim}{\upsilon}_{IN}}{\bar{\underset{\sim}{\upsilon}}_R} \right) \bar{\underset{\sim}{\upsilon}}_R \underset{\sim}{w}_R + \left(-\frac{1}{2} \left(\frac{f_R \bar{\underset{\sim}{L}}_R}{\underset{\sim}{D}_h} + K_R \right) + \frac{\underset{\sim}{L}_R}{\bar{\underset{\sim}{\upsilon}}_R^{\,2} N_{Fr}} \right) \frac{N_{\Delta h} C_1 h_{pc}}{\upsilon_{pc}} \underset{\sim}{h}_R
\end{aligned} \tag{2.53}$$

For the high heating model there are in total 6 equations with 6 dimensionless perturbed variables to investigate.

Equations:	$\underset{\sim}{M}_0$	$\underset{\sim}{M}_1$	$\underset{\sim}{M}_R$	$\underset{\sim}{E}_1$	$\underset{\sim}{E}_R$	$\underset{\sim}{I}$
Variables:	$\underset{\sim}{l}_1(t)$	$\underset{\sim}{h}_1(t)$	$\underset{\sim}{h}_R(t)$	$\underset{\sim}{w}_0(t)$	$\underset{\sim}{w}_1(t)$	$\underset{\sim}{w}_R(t)$

The next chapter will continue with the solving of these two systems of linear ordinary differential equations.

3 INVESTIGATING THE STABILITY

In chapter 2 the conservation balances were linearized for both two operational modi, which results in two sets of linear differential equations. For the high heating model there are six equations with six variables and for the low heating model there are four equations with four variables. Solving these sets of linear ordinary differential equations is the subject of this chapter.

3.1 THE MATRIX EQUATION

The sets of linear differential equations can be presented in the following form.

$$A\frac{d}{dt}\vec{x} = B\vec{x}\,, \tag{3.1}$$

where *A* stands for the matrix of coefficients for the time derivative of the variables and *B* the matrix of coefficients for the variables. $\vec{x}$ represents a column vector containing the perturbed variables. The sizes of both the matrices are 6x6 and 4x4 for the high heating model and the low heating model respectively. The resulting matrices are not displayed here due to their size, but can be found in Appendix B. The rows represent the various conservation balances and the columns represent the perturbed variables.

The solution of equation (3.1) is of the form $\vec{x} = \vec{v}e^{\lambda t}$, where the vector $\vec{v}$ contains the amplitude and phase shift of the initial perturbation. The perturbations can grow or decay exponentially in time depending on λ. When a perturbation decays exponentially in time it only has a short influence on the system and after some time the perturbation fades out. However, when the perturbations grow exponentially in time they could lead to large amplitudes in the system. The mass flow could for instance reverse or oscillate between different mass flow rates. This is considered as an instability.

Looking at the solution, stability thus depends on the value of *λ*. *λ* can have a real part as well as an imaginary part. Regarding the stability *Re(λ)* is very important, because whenever *Re(λ)>0* the perturbation grows exponentially over time resulting in an instability. Then again, when *Re(λ)<0* the perturbation decays exponentially and the system remains stable. The imaginary part of *λ* is a measure for the frequency of the oscillation of the perturbations. For an example of possible developments of the mass flow rate over time, see Figure 3.1.

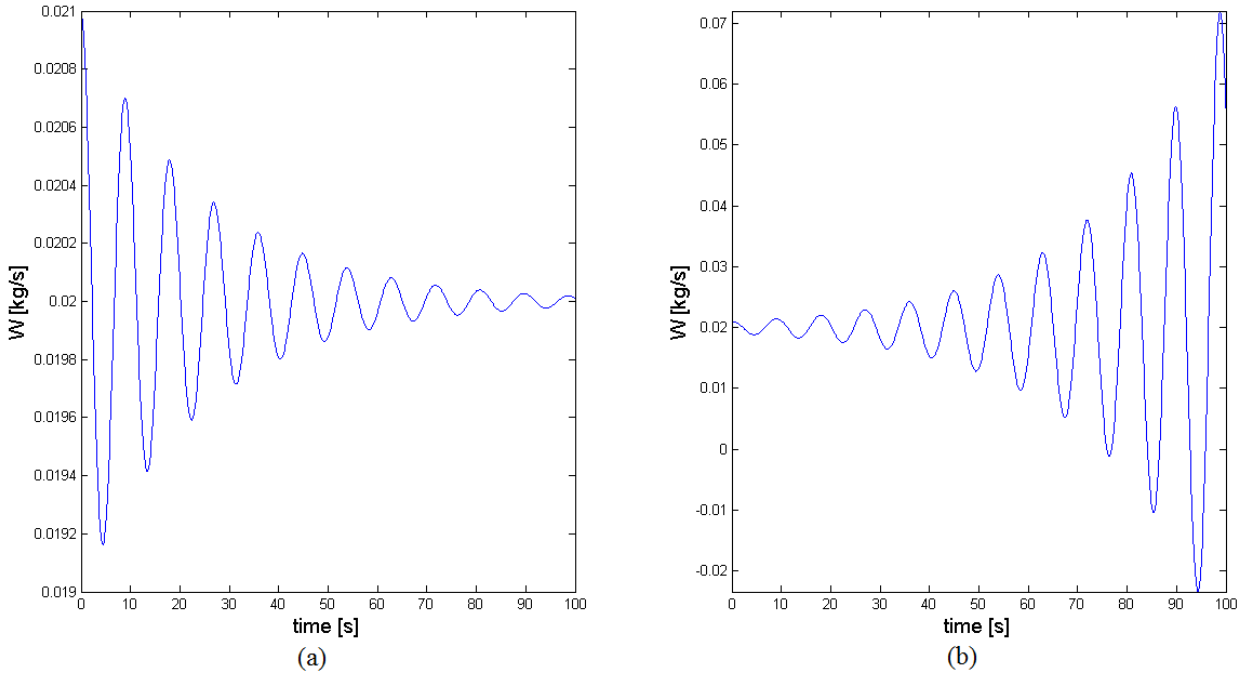

Figure 3.1: (a) Example of an exponential decay of a perturbation. (b) Example of an exponential growth of a perturbation.

3.2 SOLVING FOR LAMBDA

The main reason the stability problem is approached with a linear analysis is the simplicity of solving it. The problem can be converted to an generalized eigenvalue problem and easily be implemented into a computer code to solve for the eigenvalues. Furthermore, because the HPLWR is simplified to a water loop model with only a few nodes, very little computer power is needed to calculate the stability. These calculations can be done with a modern desktop in matter of seconds or minutes depending on the resolution of the stability maps. Another advantage of this approach is that the simplicity and computational speed enables rather quick investigation of qualitative relationships between the stability maps and various operational conditions and design parameters.

To solve for λ the solution can be substituted into equation (3.1). It is possible to rewrite this matrix equation to $A\lambda\vec{v} = B\vec{v}$, by differentiation and dividing by $e^{\lambda t}$. It is not possible to solve this by multiplying with the inverse of *A,* because *A* is singular. This now becomes a generalized eigenvalue problem which can be solved by solving $\det(B - A\lambda) = 0$. Section 4.2.4 will elaborate on the computational part of solving this equality.

3.3 DIMENSIONLESS NUMBERS

As mentioned earlier the stability maps will be derived for two operating conditions, being the inlet temperature and the power of the core. Because the HPLWR is driven by natural convection in this case the power determines the mass flow rate and is not controlled by a pump. In order to compare the stability maps of different setups two dimensionless numbers are introduced which are a measure of three operating conditions; inlet temperature, power and mass flow rate. Throughout literature there

are numerous dimensionless numbers taken as reference and a choice had to be made. In this thesis the dimensionless numbers used in T'Joen & Rohde (2012) are adopted, written in a slightly different form.

$$N_{sub} = \frac{h_{pc} - H_{IN}}{h_{pc}} \tag{3.2}$$

$$N_{\Delta h} = \frac{Q}{\bar{W} h_{pc}} \tag{3.3}$$

The subcooling number N_{sub} is as measure for the inlet temperature (specific enthalpy). Note that as the inlet temperature increases, so does the inlet enthalpy and the subcooling number decreases. The power of the core is made dimensionless in the pseudo phase change number by dividing it with the mass flow rate times the specific enthalpy at the pseudo-critical point. Although different dimensionless numbers are adopted in literature, most of them represent the same thing only differing by a factor. For instance, the pseudo phase change number is always taken as the ratio of the power of the core to the mass flow rate.

There exists a limit on the dimensionless numbers. For instance, the pseudo phase change number can not be negative, because the power is always positive resulting in a positive steady state mass flow rate. The subcooling number can only take values between 0 and 1 for this model. The inlet enthalpy can not (obviously) be negative and therefore the upper limit of N_{sub} is 1. Also the inlet enthalpy is assumed to be lower than the pseudo-critical enthalpy and this implies that the lower limit is 0 for N_{sub}. The inlet enthalpy can in fact be larger than the pseudo-critical enthalpy, but then this model has to be adapted to investigate the stability in that case.

4 COMPUTATIONAL IMPLEMENTATION

The previous two chapters have presented a mathematical model and a method to solve for the stability. Next, the implementation of the mathematical model in *Matlab* is discussed. The built up of the code is elaborated and choices that had to be made during the coding are explained. Furthermore, the methods to investigate frequencies and Ledinegg instabilities are stated as well.

4.1 OVERALL CONSIDERATIONS

The goal was to write a code which represents robustness and structure. A code has to be flexible for different input parameters and resolutions (regarding stability maps). During the coding the computational speed was always kept in mind, but because the water loop is divided into only a few nodes the problem does not require a large amount of calculations. Hence, the emphasis is not on the computational speed but more on readability. Stability maps with a high resolution can be made within minutes. Furthermore, *Matlab* is designed for matrix operations and, therefore, vectorization of code can be quite useful for the computational speed as FOR loops can be avoided.

4.2 THE CODE

This section will cover all the elements of the code that were implemented in order to plot a stability map. For every combination of inlet enthalpy and power of the core the stability is calculated.

4.2.1 THE GENERAL ALGORITHM

First of all, the goal was to derive a stability map that can vary in resolution (in N_{sub} and $N_{\Delta h}$). Instead of assigning a range for the power, which would result in unequal steps for $N_{\Delta h}$, the range and resolution for $N_{\Delta h}$ (and N_{sub}) are determined beforehand. If for both the dimensionless numbers the same number of steps is assigned, the stability map will have *NxN* grid points. This is the case in most of the stability maps in chapter 5. Both the dimensionless numbers are set to begin at a value close to zero (for instance 0.001). Because according to the model, the pseudo-critical point should be inside the core section. From the subcooling number the inlet enthalpy can be easily calculated. The calculation for the steady state mass flow rate and the power is less straight forward, which will be discussed later on.

The general structure to calculate the stability is as follows, see Figure 4.1. Two FOR loops are implemented in order to calculate the stability for every combination of N_{sub} and $N_{\Delta h}$. The first FOR loop varies the subcooling number and the second FOR loop varies the pseudo phase change number. Within the second FOR loop an IF statement is used to distinguish between the high heating and the low heating model. From the steady state solutions, see section 4.2.2, it becomes clear that for $N_{\Delta h}<N_{sub}$ the length L_0 becomes larger than the length of the core, which is impossible. The low heating model is therefore used for $N_{\Delta h}\leq N_{sub}$ and the high heating model for $N_{\Delta h}>N_{sub}$.

For each combination of N_{sub} and $N_{\Delta h}$ the stability is calculated and a matrix is built with ones and zeros. The number 1 represents a stable point and the number 0 represents an unstable point. The stability

matrix is then plotted against N_{sub} and $N_{\Delta h}$ using the function IMAGESC, which plots an image of a matrix using colors. In this case the color red indicates an unstable point and blue a stable one.

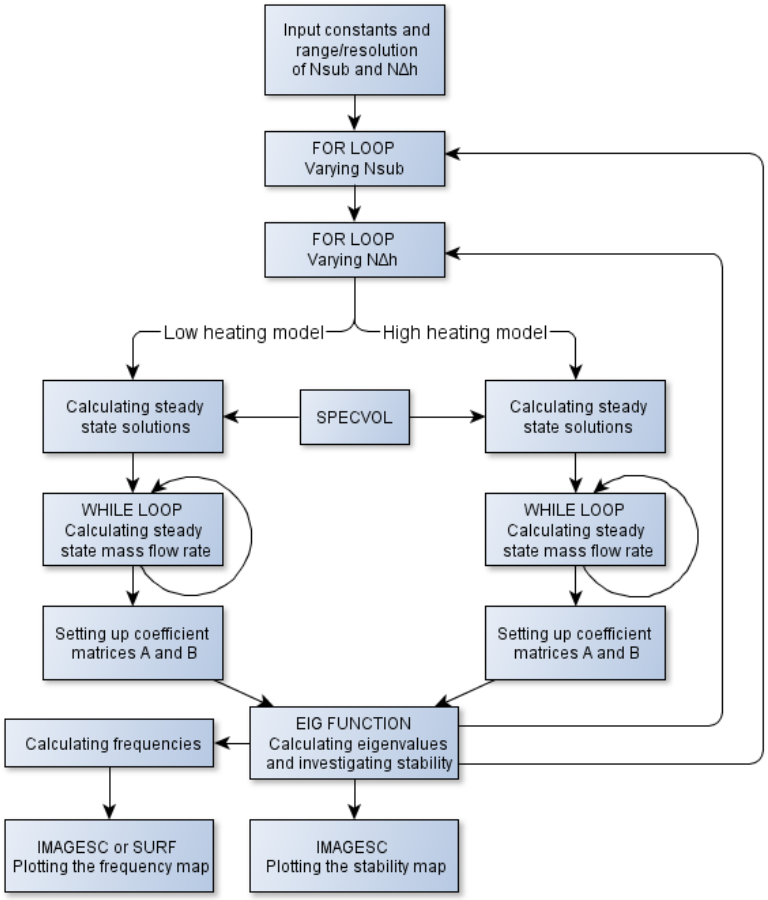

Figure 4.1: Flowchart of the *Matlab* script. The calculation of the eigenvalues is done for every combination of N_{sub} and $N_{\Delta h}$ with two FOR loops. An IF statement is used to make the distinction between the low heating and high heating model.

4.2.2 THE STEADY STATE SOLUTIONS OF THE ENTHALPY AND LENGTH OF NODE 1

The coefficient matrices *A* and *B* have to be set up and therefore a number of constants and steady state solutions have to be determined first. The *Matlab* script begins with assigning all the constants independent of the operating conditions, i.e. geometry, pressure loss coefficients, pseudo-critical data of water etc. Then there are also the steady state solutions in the coefficient matrices which are dependent on the operating conditions. These solutions are assigned in the second FOR loop, because these depend on the dimensionless numbers.

The following steady state solutions are derived from the equations given in chapter 2 by setting the derivatives to zero and substituting N_{sub} and $N_{\Delta h}$ into the equations. For the high heating model the steady state solutions for L_1 and H_1 are given in equation (4.1) and (4.2) and are derived from the conservation balances (2.33) and (2.34).

$$\bar{L}_1 = L\left(1-\frac{N_{sub}}{N_{\Delta h}}\right) \qquad \left(N_{\Delta h} > N_{sub}\right) \tag{4.1}$$

$$\bar{H}_1 = h_{pc}\left(1+N_{\Delta h}\frac{\bar{L}_1}{L}\right) \qquad \left(N_{\Delta h} > N_{sub}\right) \tag{4.2}$$

There is no energy added or lost in the riser and, therefore, the steady state enthalpy H_R is the same as H_1, which also follows from the steady state solutions. Note that the time dependent enthalpies are not the same, because the riser comes after the core and there is a delay between the riser and the core due to the finite mass flow rate. The steady state solution for the outlet enthalpy H_{out} is derived from conservation balance (2.7) and applies to the low heating model.

$$\bar{H}_{out} = H_{IN} + h_{pc}N_{\Delta h} \qquad \left(N_{\Delta h} \le N_{sub}\right) \tag{4.3}$$

Again, the riser does not change the enthalpy and, therefore, $\bar{H}_R = \bar{H}_{out}$. With these steady state solutions the remaining steady state variables $\bar{L}_0$, $\bar{\upsilon}_1$, $\bar{\upsilon}_R$, $\bar{H}_0$, $\bar{\upsilon}_0$ and $\bar{\upsilon}_{out}$ can be calculated using the equations given in chapter 2 and the equation of state, i.e. equation (2.1). Because the steady state outlet enthalpy of the core is the same as the steady state enthalpy of the riser the steady state specific volumes are also the same. Thus $\bar{\upsilon}_R = \bar{\upsilon}_{out}$ and $\bar{\upsilon}_R = \bar{\upsilon}_1$ for the low- and high heating model respectively.

The equation of state is implemented with the use of a function named SPECVOL. This function has as input the steady state enthalpy and as output the steady state specific volume. The two linear approximations are distinguished with the use of an IF statement. The boundary between these two approximations lies at the pseudo-critical point.

4.2.3 THE STEADY STATE MASS FLOW RATE

The only steady state variable that remains then is the steady state mass flow rate. In chapter 2 $\bar{W}$ is given for both the high- and low heating model. All the steady state variables that are needed for this expression are calculated before and can be substituted. The friction factor, *f*, is called the Darcy friction factor and can be approximated with the formula of Blasius, which depends on the Reynolds number (Janssen & Warmoeskerken, 1997). It can also be set as a constant, but using Blasius leads to a more accurate approximation of the Darcy friction factor. The Reynolds number turns out to be in the range applicable to the Blasius relation.

$$f = 0.316\,\mathrm{Re}^{-\frac{1}{4}} \qquad (4000 < \mathrm{Re} < 10^5) \tag{4.4}$$

$$\mathrm{Re} = \frac{\bar{W}D_h}{A\mu} \tag{4.5}$$

The Reynolds number is a function of the mass flow rate itself, so *Re* can not be written down in an explicit form. Hence, an iteration process is needed to calculate $\bar{W}$ and a WHILE loop is introduced, see Figure 4.1. The iteration process stops when the new calculated value of the mass flow rate differs $1\cdot10^{-9}$ % from the previous calculated value. The value of the dynamic viscosity present in the Reynolds number

is a function of enthalpy. However, there was chosen to approximate the dynamic viscosity with a constant value of μ_{pc}=4.27975·10^{-5} for simplicity. This implies that the resulting friction factors are the same for each node. For working temperatures of 280°C to 500°C this approximation of the dynamic viscosity leads to a maximum possible deviation of 20% in the calculated Darcy friction factors. After $\overline{W}$ is known, the Froude number can be calculated.

4.2.4 THE EIGENVALUE PROBLEM

Now that the steady state solution and (thus) the constants are known, the solving of the generalized eigenvalue problem can begin. The coefficient matrices *A* and *B* are set up for each of the two models. The matrices can be looked up in Appendix B. To solve a generalized eigenvalue problem QZ factorization is needed if *A* is singular, which is the case here. The EIG function in *Matlab* uses the QZ factorization to solve $\det(B - A\lambda) = 0$ (Matlab, 2013). The size of the square matrices determines the number of eigenvalues. In the high heating model six eigenvalues are found and in the low heating model four. However, in most cases there are eigenvalues which are infinite because *A* is singular. The degree of the determinant is then smaller than the size of the matrices. So in general there are *r* finite eigenvalues and *n-r* infinite eigenvalues, where *r* is the degree of the determinant (Wolfram, 2013). Koren (2010) had the same problem with these infinite eigenvalues and found out that *Matlab* returns these infinite eigenvalues if there are equivalent eigenvalues in the solution of the characteristic polynomial of the determinant. So an infinite eigenvalue means that that eigenvalue corresponds to another eigenvalue with the same value. Koren (2010) gave a simple test case in his appendix demonstrating this problem. If we know that these eigenvalues are equivalent to other eigenvalues these eigenvalues can be disregarded, because for the stability problem we only want to know if one of the eigenvalues is positive. And because the infinite eigenvalues are copies of other eigenvalues they do not provide additional information about the stability. For this reason all eigenvalues larger than 10^{12} are neglected. After that, the real part of the remaining eigenvalues are analyzed for their sign. If one of the real parts of the eigenvalues is positive, a zero is set for that cell in the stability matrix indicating an unstable point. If all the eigenvalues are negative that combination of N_{sub} and $N_{\Delta h}$ is considered stable and an 1 is assigned to the matrix cell.

4.3 RESONANCE FREQUENCIES

To investigate the frequencies of the response to perturbations the imaginary parts of the eigenvalues become important. Hence, it is worth to have a closer look to the form of the solution. The solution is of the form $\vec{x} = \vec{v}e^{\lambda t}$ and can be decomposed as following, done by Koren (2010).

$$v_k = \alpha_k e^{i\beta_k} \qquad \text{where } \alpha_k = |v_k| \text{ and } \beta_k = \angle v_k \tag{4.6}$$

$$\lambda = a + ib \qquad \text{where } a = \mathrm{Re}\{\lambda\} \text{ and } b = \mathrm{Im}\{\lambda\} \tag{4.7}$$

α_k and β_k represent the amplitude and phase shift of the initial introduced perturbation respectively. *a* represents the growth (or decay) rate of the development of the perturbation and *b* represents its frequency. The solution can be written as:

$$x_k = \alpha_k e^{at} e^{i(\beta_k + bt)} \tag{4.8}$$

Single imaginary eigenvalues in the solution of the generalized eigenvalue problem would result in an imaginary development of the perturbation, which is impossible in a physical system. Therefore, in the solution of the characteristic polynomial another eigenvalue is present with the same real part and opposite sign of the imaginary part. These two eigenvalues will result in the formation of a sinusoid, written as follows:

$$\alpha_k e^{at}\left(e^{i(\beta_k + bt)} + e^{-i(\beta_k + bt)}\right) = 2\alpha_k e^{at}\cos\left(\beta_k + bt\right) \tag{4.9}$$

The initial phase shift is not important in this research, but the imaginary part of λ gives the frequency of the development of the perturbation. The imaginary part of the eigenvalue is found by first filtering all the positive eigenvalues, because when the real part of an eigenvalue is negative the perturbation fades out. Frequencies of negative eigenvalues are not investigated in this research. Subsequently, the frequency of the eigenvalue with the largest positive real part, representing the most dominant perturbation, is taken as reference for the frequencies. The time t is made dimensionless during the derivation of the mathematical model and therefore the frequencies are dimensionless too. The frequency with dimension is assigned to the matrix cell corresponding with N_{sub} and $N_{\Delta h}$. The frequency spectrum of the stability domain can be plotted in two ways. A 3-dimensional plot can be made with the SURF function which gives a good impression of the absolute value of the frequencies and the relative size throughout the stability domain. And a 2 dimensional plot can be made with the IMAGESC function, which can be overlaid with the regular stability map to see where frequencies are relatively high and where instability without frequencies occurs.

4.4 LEDINEGG INSTABILITIES

As explained in section 1.3, Ledinegg instabilities occur when the mass flow rate changes abruptly to another mass flow rate. The mass flow rate versus power characteristics were investigated for different subcooling numbers and it turned out that for some subcooling numbers three different mass flow rates could exist for one and the same power. A Ledinegg instability could occur at those power inputs, because the mass flow rate can shift to one of the other two mass flow rates. In Figure 4.2 three characteristics are plotted for three different subcooling numbers and between the two red lines three mass flow rates exist for one power input at N_{sub}=0.95. The kink present in the characteristics, most clearly visible in the N_{sub}=0.95 characteristic, is caused by the transition from the low heating model to the high heating model. At the kink the pseudo-phase-change number equals the subcooling number. The calculation for the mass flow rate switches then from equation (2.13) to equation (2.37).

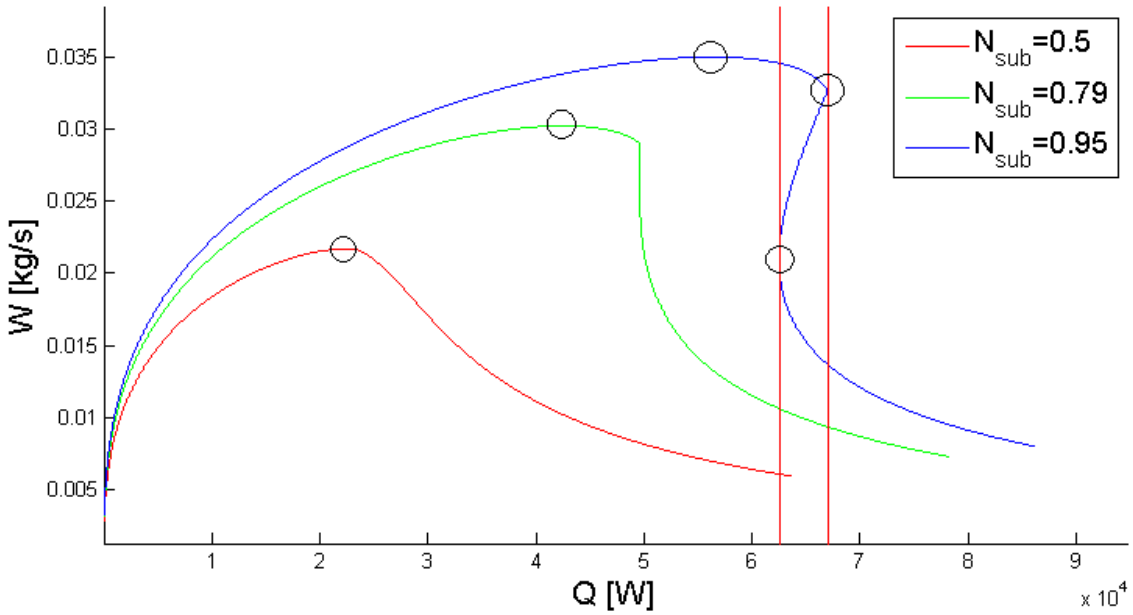

Figure 4.2: Mass flow rate versus power for three different subcooling numbers. The red lines indicate the region where more than one mass flow rate could exist for the same power input. Sign swaps are indicated with circles. For higher subcooling numbers multiple mass flow rates exist for a certain power range.

One method to find the boundaries indicated with the red lines is by calculating the slope of the characteristic. The slope changes sign three times in the characteristic with N_{sub}=0.95, encircled points on the characteristic, and by finding the sign swaps the boundaries can be found for $N_{\Delta h}$. Only the last two sign swaps are important, because the first one occurs at the maximum of the characteristic. Because *Matlab* uses a discrete representation of a continuous variable a finite difference method must be used to calculate the slope. There was chosen to approximate the slope with a central difference approximation, see equation (4.10).

$$\frac{d\bar{W}_n}{dQ_n} \approx \frac{\bar{W}_{n+1} - \bar{W}_{n-1}}{Q_{n+1} - Q_{n-1}} \tag{4.10}$$

A vector with the slopes at each point, except for the first and last point, is then obtained and checked if the sign of the slopes swaps more than one time. Because for lower subcooling numbers there are not any powers with multiple mass flow rates and only one sign swap occurs at the maximum of the characteristic. The appearance of multiple mass flow rates starts from N_{sub}=0.79. When multiple mass flow rates exist the index numbers of the power vector at the last two points (see Figure 4.2) are used to indicate the two limits for the range of $N_{\Delta h}$ where this occurs, see Figure 4.3. This can then be plotted in a new stability map where the occurrence of Ledinegg instabilities is indicated, see chapter 5.

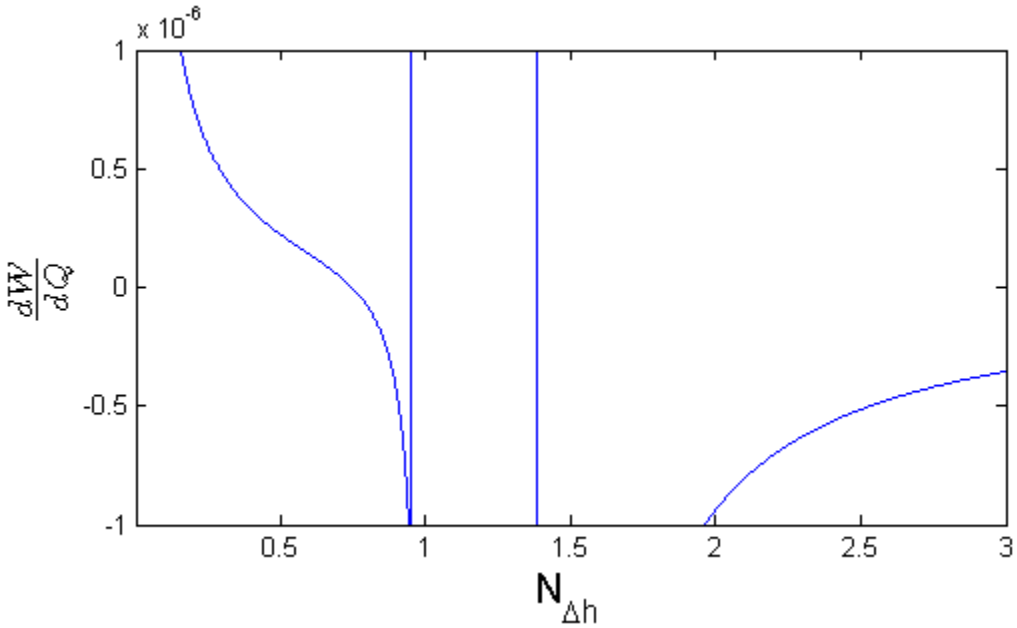

Figure 4.3: The slope plotted against $N_{\Delta h}$ for N_{sub}=0.95. At three different points the sign of the slope swaps from negative to positive or vice versa. The last two sign swaps are used to indicate the range of $N_{\Delta h}$ where Ledinegg instabilities occur.

5 RESULTS

The mathematical model has been computationally implemented and the results are presented and investigated in this chapter. First, a parametric study will be done to investigate what kind of influence the design parameters have on the stability maps. A comparison will be made with the parametric studies from Van Bragt (1998) for a natural circulation driven BWR and from Ortega Gomez (2009) for a single pass HPLWR driven by pumps. Subsequently, Ledinegg instabilities are investigated with the use of the steady state solutions of the mass flow rate and frequency maps. The results are compared to results obtained by Guido et al. (1991) for a single boiling water channel.

5.1 PARAMETRIC STUDY

The design parameters have an influence on the stability map of a natural circulation driven supercritical water loop. In Table 5.1 an overview is given of the influences of various design parameters on the stability of the system. This table has the same format as the table presented in Ortega Gómez (2009) for easy comparison. A stabilizing effect is denoted with a "+" and a destabilizing effect with a "-". The arrows indicate an increase or decrease of the design parameter. The next subsections will elaborate on each design parameter. The different instable regimes in the stability plots are identified if possible.

Table 5.1: Influence of different design parameters on the stability map of the supercritical water loop. A stabilizing effect is denoted with a "+" and a destabilizing effect with a "-".

Design parameter	**Variation ↑**	**Variation ↓**
Volume buffer vessel	+	-
Length riser	-	+
Length core	-	+
Hydraulic diameter	+	-
Inlet core pressure loss coefficient	+	-
Downcomer pressure loss coefficient	+	-
Riser pressure loss coefficient	-	+

5.1.1 REFERENCE CASE

First, the stability map that was obtained with the *Matlab* script is displayed for design parameters that will be taken as reference in this chapter, see Figure 5.1 and Table 5.2. In the caption of the upcoming figures the design parameters that deviate from the standard design parameters are given for that specific stability map.

Table 5.2: Design parameters taken as standard in this research.

Design parameter	Value
Volume buffer vessel	10 dm^3
Length of riser	4.2 m
Length of core	4.2 m
Hydraulic diameter channel	5.6 mm
Flow area	35.5 mm^2
Inlet core pressure loss coefficient	1
Downcomer pressure loss coefficient	1
Riser pressure loss coefficient	20

The N_{sub}=$N_{\Delta h}$ line is the boundary where the mathematical model makes the switch between the low heating model and the high heating model. Above this boundary the stability is calculated with the low heating model and below this boundary the high heating model is used. The sharp transition from stable to unstable at N_{sub}=$N_{\Delta h}$ can be explained with the equation of state. The approximation for the equation of state used in this thesis is a rather crude approximation, because the equation of state is split up into two different approximations, separated by the pseudo-critical point. The approximation is not continuous at the pseudo-critical point and could explain the sharp transition from stable to unstable at the N_{sub}=$N_{\Delta h}$ line.

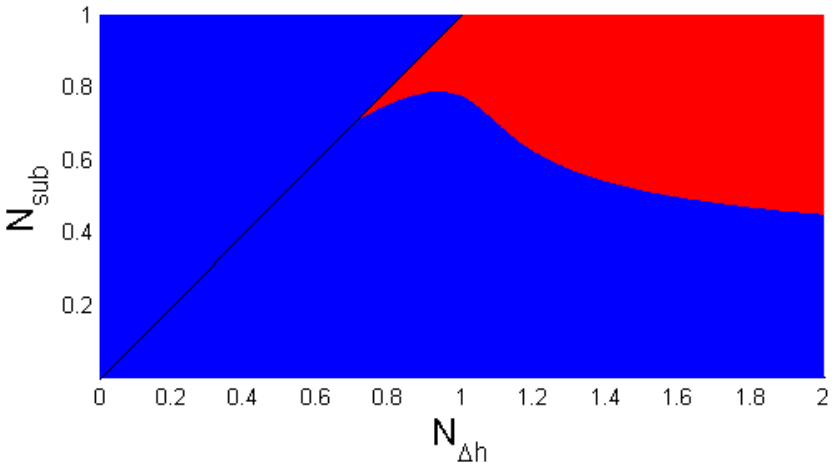

Figure 5.1: Stability map for the standard design parameters as listed in Table 5.2. Red indicates the unstable domain and blue the stable domain. The black line indicates the N_{sub}=$N_{\Delta h}$ line.

5.1.2 VOLUME OF THE BUFFER VESSEL

It became soon quite clear that the instability domain is highly dependent on the volume of the buffer vessel. As the volume increases the instability domain becomes smaller and the system becomes more stable. In Figure 5.2 three neutral stability boundaries are plotted for three different volumes of the buffer vessel. The neutral stability boundary (NSB) is the boundary where the transition from stable to unstable takes place, above and right of the NSB the system is unstable and below and left of the NSB the system is stable. The system becomes more stable for a higher volume of the buffer vessel, because any growing perturbations in the core or riser will fade out in the relatively large bulk of water in the buffer vessel. This can be related back to the linearized momentum balance, see equations (2.27) and (2.53). The volume of the buffer volume is present before the $\frac{d}{dt}\underset{\sim}{w}_0$ term and is proportional to the average time that the water flows through the buffer vessel. If the volume increases, the mass flow rate w_0 is strongly delayed with respect to the inlet mass flow rate and any oscillating perturbations fade out. The buffer vessel therefore acts like an attenuator in the water loop, large amplitudes of perturbations are damped out and are not present in the downcomer afterwards.

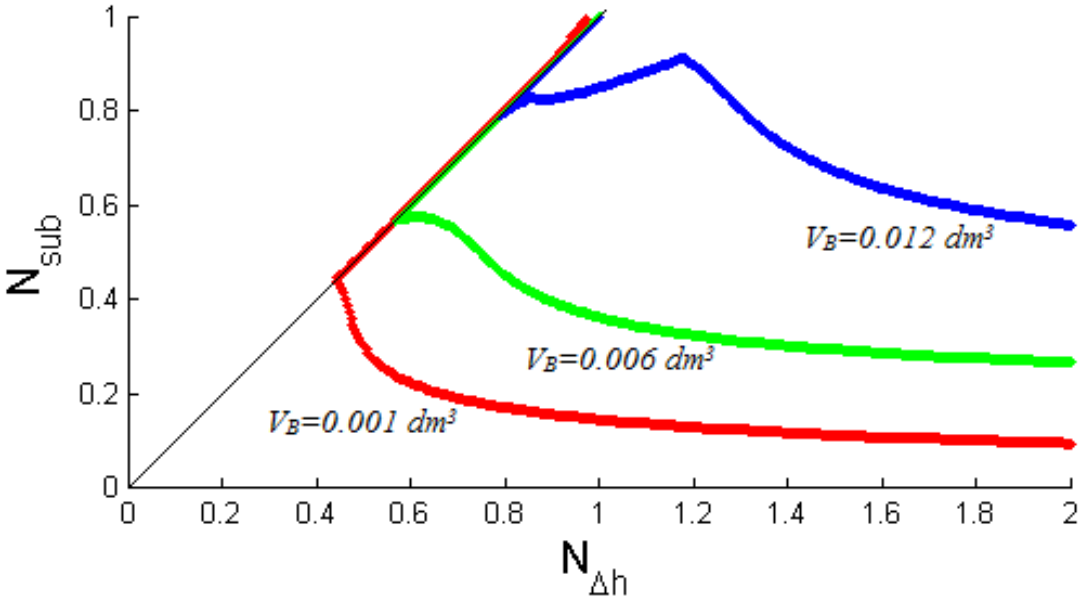

Figure 5.2: Neutral stability boundaries for different volumes of the buffer vessel. As the volume increases the instability domain becomes smaller. The unstable region lies to the right of the NSB. The black line indicates the N_{sub}=$N_{\Delta h}$ line.

Something else was also noticed when investigating the influence of the buffer vessel on the stability. As the volume increases, the instable region around N_{sub}=0.9 and $N_{\Delta h}$=1.1 remains the same, even for relatively high volumes. This region is also present in the stability maps for small volumes of the buffer vessel, but is surrounded by other type of instabilities. Figure 5.3 shows the stability map for a system with a volume of 1 m^3 for the buffer vessel, a thousand times higher than in the case with the red NSB in Figure 5.2. These instabilities are not dynamic, but they turn out to be Ledinegg instabilities (see section 5.2) and remain constant when the volume of the buffer vessel is further increased. Ledinegg instabilities can be found with the steady state equations as mentioned in section 4.4. Equation (2.37) and (2.13)

show no dependence on the volume of the buffer vessel and therefore this instability domain remains, even when the volume is increased to high values.

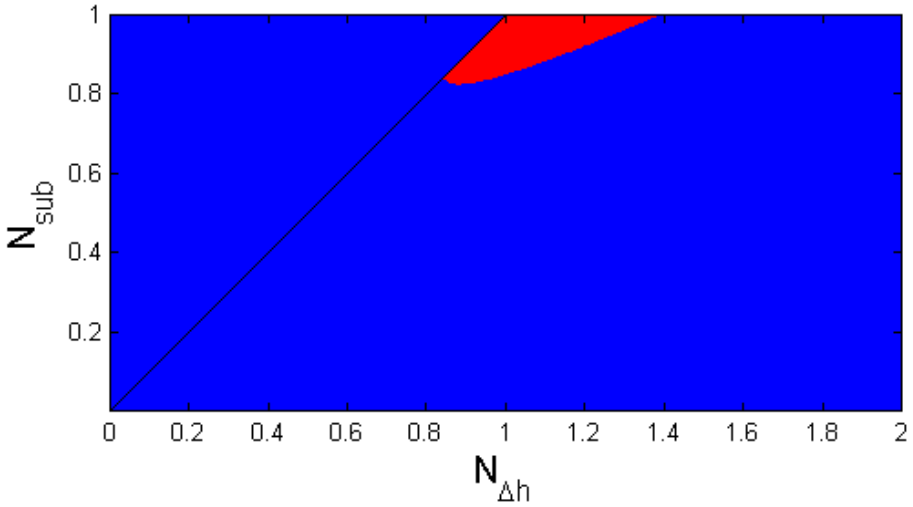

Figure 5.3: Stability map for a system with a buffer vessel volume of 1 m^3. One instability domain (indicated with red) remains regardless the volume of the buffer vessel. The black line indicates the N_{sub}=$N_{\Delta h}$ line.

5.1.3 RISER LENGTH

Van Bragt (1998) investigated the influence of the length of the riser on the stability of a natural circulation driven water loop in a BWR. In Figure 5.4 his plot of three neutral stability boundaries for three different lengths of the riser is presented.

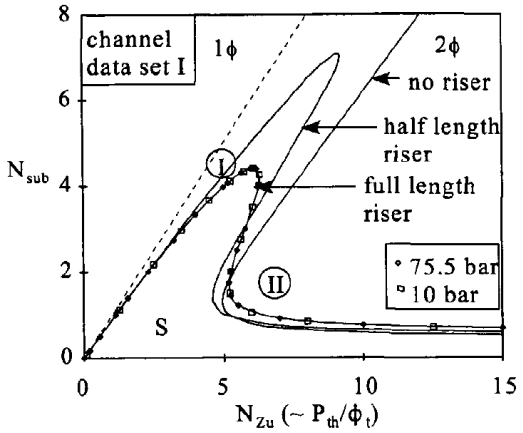

Figure 5.4: Three different NSB's plotted for a BWR with different risers lengths. Dimensionless numbers are comparable with the ones used in this study. *S* indicates the stable domain and the I and II indicate the different types of dynamic instabilities. As the riser length increases the system destabilizes. Source: (Van Bragt, 1998).

The dimensionless numbers used in his research are quite similar and differ only by a factor:

$$N_{Zu} = \frac{q' L_C}{\phi_t \left(h_g - h_f\right)} \frac{\rho_f - \rho_g}{\rho_g}, \qquad N_{sub} = \frac{h_f - h_{l_{C,i}}}{h_g - h_f} \frac{\rho_f - \rho_g}{\rho_g} \tag{5.1}$$

The subscripts *g* stands for vapor and *f* for saturated liquid. N_{Zu} is comparable with $N_{\Delta h}$, because it is also proportional with power over mass flow (indicated with red) and the subcooling number increases when the inlet enthalpy (indicated with red) decreases, which is the same as in this research. Although the BWR is different from the HPLWR the influence of the riser can be compared, because in both systems the density decreases rapidly as the enthalpy increases. As can be seen in Figure 5.4, when a riser is introduced to the system, another type of instability emerges, a Type-I instability. These instabilities are caused by the gravitational pressure drop in the riser (Van Bragt, 1998) and as the length of the riser increases the NSB is pushed downwards in the stability plot.

Figure 5.5 shows the NSB's for different riser lengths for the model used in this research. Compared with the plot of Van Bragt (1998) the increase of the riser length has a similar influence on the stability. As the length of the riser increases the NSB lowers in the stability map. When no riser is implemented the NSB draws away to the right, similar to the results found in Van Bragt (1998). Only a small instability domain remains, same as in Figure 5.3, these are however caused by Ledinegg instabilities which will be discussed further in section 5.2. When the riser length increases, Type-I instabilities become more dominant and force the NSB downwards. Type-I instabilities can be explained as follows. A perturbation is introduced in the mass flow at the core inlet, for instance a small increase. This will result in less heating of the mass flow and a lower core outlet enthalpy, assuming constant power input of the core. The resulting higher density at the outlet of the core and in the riser will decrease the gravitational pressure drop between the riser and the downcomer and therefore the mass flow rate decreases. Subsequently, the core will heat up the mass flow more and the outlet enthalpy increases. The exact opposite process continues and will result in an increase of the mass flow rate, starting again at the beginning of the cycle. These oscillations are amplified when the length of the riser becomes greater, because the gravitational pressure drop increases. This results in an instability when the amplitude of the oscillations grow in time instead of decaying. So the lowering of the NSB for an increasing riser length is an indication that Type-I instabilities play an important role in the stability of the natural circulation driven supercritical water loop.

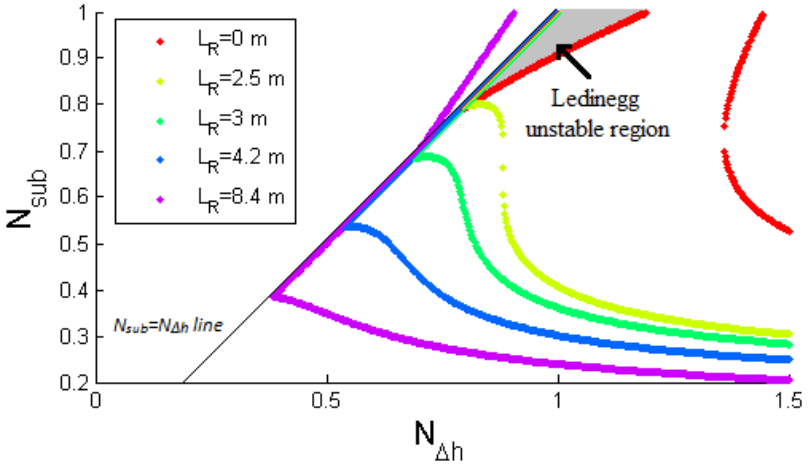

Figure 5.5: Five different NSB's are plotted for different lengths of the riser. V_B=5 dm^3. As the length of the riser decreases the instability domain shifts more to the upper right part of the stability map. The unstable region lies to the right of the NSB. The black line indicates the $N_{sub}=N_{\Delta h}$ line. The gray area indicates the Ledinegg unstable region for the stability map with L_R=0 m.

Furthermore, investigating the frequencies of the stability map can give more insight about the nature of the instabilities that occur. Figure 5.6 presents the frequency map for the stability map of a system with riser length L_R=4.2 m. As can be seen the lower right part of the instability domain has higher frequencies than the upper left instability domain. One part of the instability domain does not have a frequency, which is partly caused by Ledinegg instabilities (further investigated in section 5.2). Type-II instabilities are known to have higher frequencies than Type-I instabilities (Van Bragt, 1998). So the presumption that the upper left part of the instability region are Type-I instabilities is supported by the frequency map.

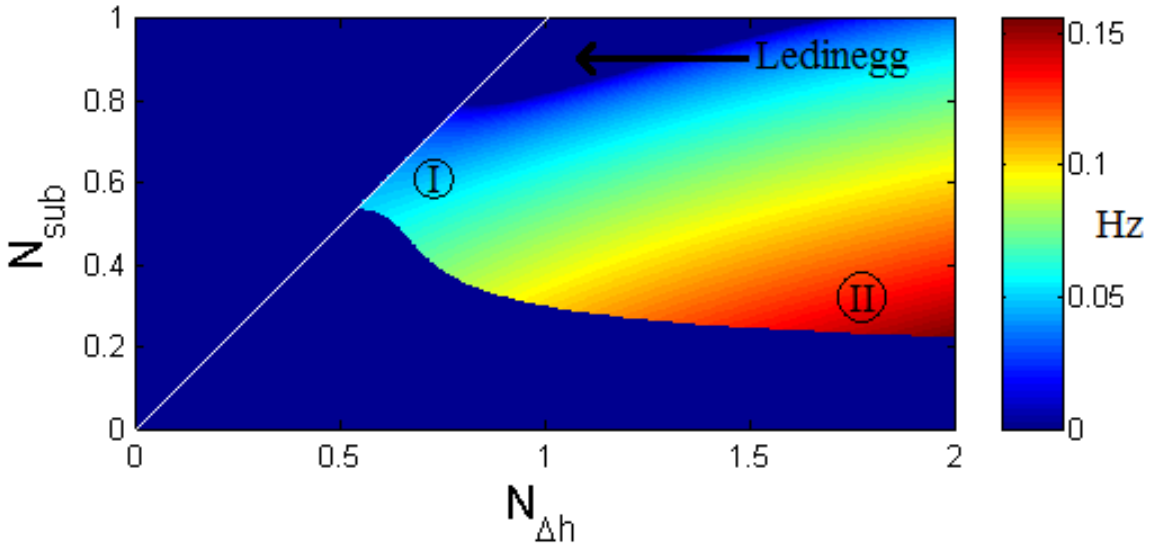

Figure 5.6: Frequency (Hz) stability map. L_R=4.2 m and V_B=5 dm^3. The lower right part of the instability domain has higher frequencies than the upper left part which could denote the distinction between Type-I instabilities and Type-II instabilities. The part without frequencies are non-dynamic instabilities and are partly caused by Ledinegg instabilities. The white line indicates the N_{sub}=$N_{\Delta h}$ line.

5.1.4 LENGTH CORE AND HYDRAULIC DIAMETER

The length of the core and the hydraulic diameter have opposite influences compared with the results presented by Ortega Gómez (2009), who investigated the influences of the design parameters for a HPLWR driven by a pump. An increase of the heated length and a decrease of the hydraulic diameter stabilizes a HPLWR driven by a pump, but the opposite was found in this study for a natural circulation driven HPLWR. The influences of both design parameters have the same physical explanation and are therefore explained together in this section.

The Type-I instabilities stabilize when the length of the core increases and the hydraulic diameter decreases, but the lower right area of the instability domain destabilizes (region around N_{sub}=0.4 and $N_{\Delta h}$=1.2), see Figure 5.7. The lower right part probably consists of Type-II instabilities, because Type-II instabilities are caused by the frictional pressure drops (Van Bragt, 1998). And as can be seen in the momentum equations (2.36) and (2.12) the friction terms become larger for a higher length of the core and a lower hydraulic diameter. However, the stability of the system depends on which friction term increases the most. An inlet restriction of a boiling channel results in a damping effect of increasing flow

and therefore has a stabilizing effect. An outlet restriction on the other hand has a destabilizing effect, because it slows the flow down and may become out of phase with the change of inlet flow (Boure, Bergles, & Tong, 1973). Decreasing the hydraulic diameter results in an increase of all friction terms due to wall shear, but because of the lower density in the riser the outlet friction increases more than the inlet friction and the system destabilizes, see equation (2.36). The same holds for the length of the core, because an increase also implies an increase of the friction in node 1. The friction in node 1 can be considered as an outlet restriction, because the flow has surpassed the pseudo-critical point in that node. And because the specific volume of node 1 is greater than in node 0, the friction in node 1 increases more than the friction in node 0 and, therefore, the system destabilizes. The frequency maps confirm this result. They indicate that the higher frequencies lie in the indicated Type-II instability region and the lower frequencies in the Type-I instability region.

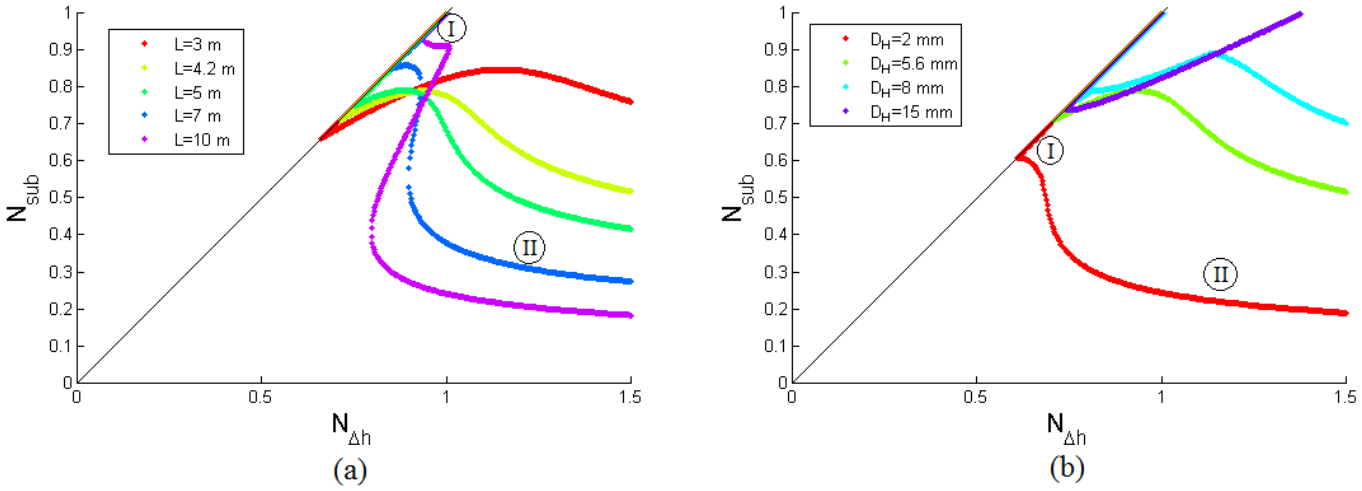

Figure 5.7: (a) NSB's for different core lengths. (b) NSB's for different hydraulic diameters. As the length of the core increases and the hydraulic diameter decreases the Type-II instability region increases. The black line indicates the N_{sub}=$N_{\Delta h}$ line.

5.1.5 OUTLET AND INLET RESTRICTIONS

The pressure loss coefficients have the same influence as found by Ortega Gómez (2009). The inlet pressure loss coefficient K_R has a destabilizing effect and the inlet pressure loss coefficients K_D and K_0 have a stabilizing effect. The pressure loss coefficient K_1 in the high heating model is set to zero, because assigning a value would result in a discontinuous mass flow rate at the N_{sub}=$N_{\Delta h}$ boundary. The low heating model does not include this pressure loss coefficient and therefore the mass flow rate for the high heating model would be lower than the mass flow rate of the low heating model if K_1 is not zero. Pressure losses in the heavy liquid region have a stabilizing effect and pressure losses in the light liquid region have a destabilizing effect (Ortega Gómez, 2009). K_0 and K_D are both present in the heavy liquid regions of the supercritical water loop and therefore have a destabilizing effect, see Figure 5.8. The inlet pressure loss coefficient of the riser can be considered as an outlet pressure loss coefficient of the core and is present in the low density region. This pressure loss coefficient therefore destabilizes the system, see Figure 5.9.

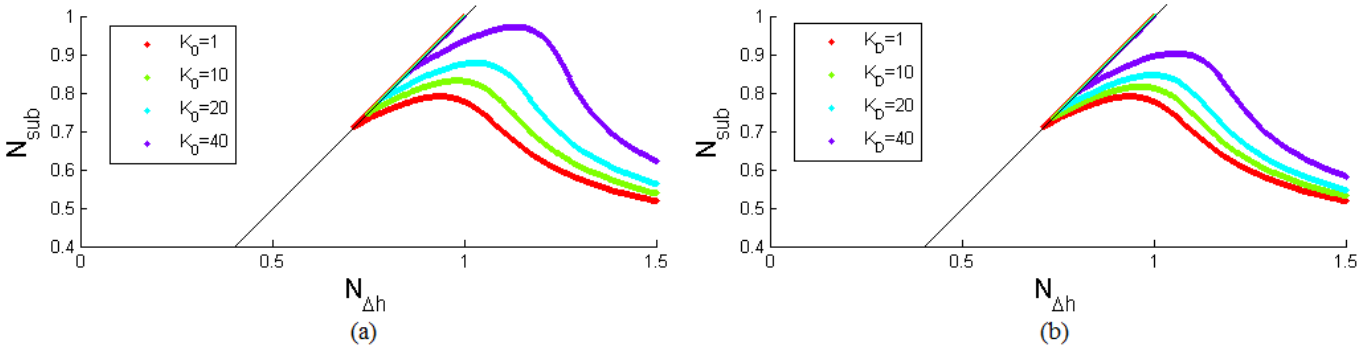

Figure 5.8: (a) Inlet core pressure loss coefficient. (b) Downcomer pressure loss coefficient. When both of the inlet pressure loss coefficients are increased the system stabilizes. The black line indicates the N_{sub}=$N_{\Delta h}$ line.

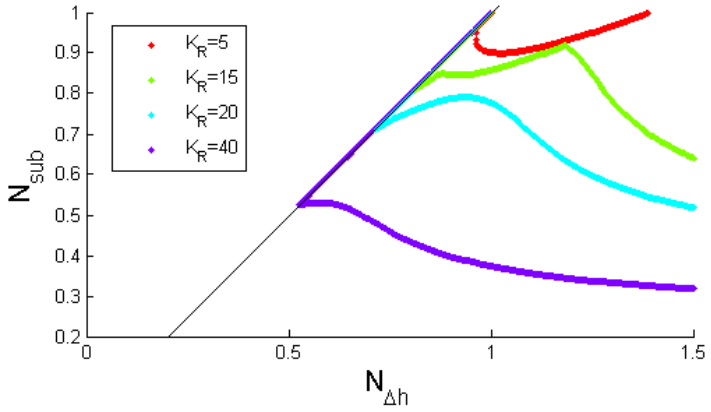

Figure 5.9: Inlet riser pressure loss coefficient. This pressure loss coefficient lies in the low density region and therefore destabilizes the system. The unstable region lies to the right of the NSB. The black line indicates the N_{sub}=$N_{\Delta h}$ line.

5.2 LEDINEGG INSTABILITY

Some stability maps for different design parameters looked very similar to earlier found stability maps by Guido et al. (1991). This resemblance created the presumption that Ledinegg instabilities are also present in the stability maps of a SCWR in this research. Guido et al. (1991) approached the stability problem analytically for parallel boiling water channels as well as for a single heated channel. In Figure 5.10 two stability maps are presented, one calculated by Guido et al. (1991) for a single boiling water channel and the resembling stability map found in this research for a supercritical water loop without a riser. Again the dimensionless number are comparable and differ by a factor. The straight dashed line indicates the boundary of the Ledinegg unstable region in Figure 5.10a.

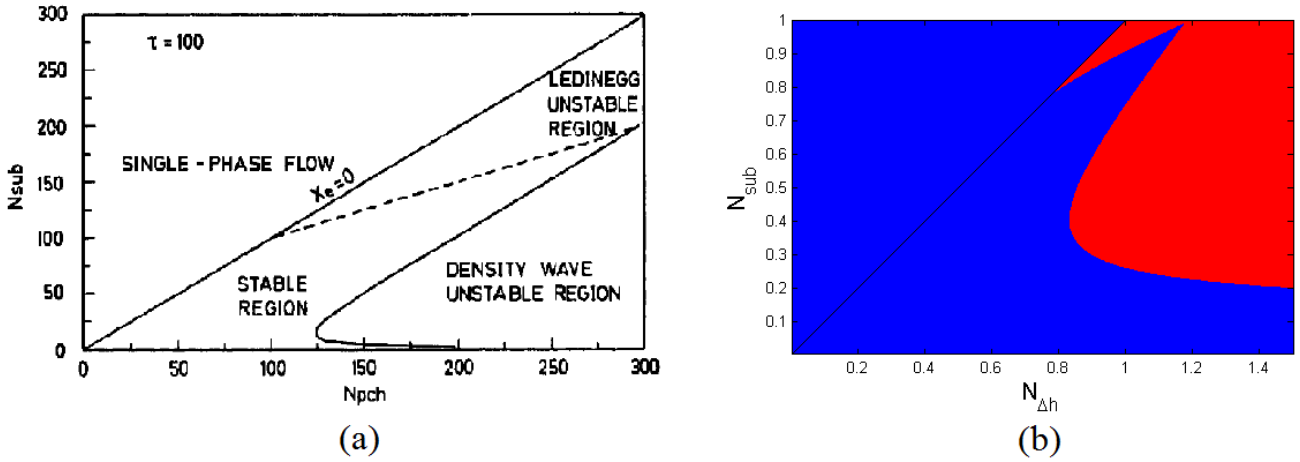

Figure 5.10: (a) Stability map derived for a single heated channel. τ is a friction parameter and the X_e=0 line represents the boundary between single-phase and two phase flow. Source: (Guido, Converti, & Clausse, 1991). (b) Stability map showing a comparable straight line in the NSB. V_B=2 dm^3, L_R=0 m. The black line indicates the N_{sub}=$N_{\Delta h}$ line.

To investigate if Ledinegg instabilities are present in the stability maps the flow rate versus power characteristics are investigated as explained in section 4.4. Certain combinations of mass flow rate and power turn out to be unstable and lie in the region indicated with the black line, which corresponds to a range of $N_{\Delta h}$ and is indicated in Figure 5.11 with a black line. This range corresponds to the points where more than one steady state solution is found for one power (indicating that a system may swap from one solution to the other when perturbed). The other two blue lines between the red boundaries are stable regions. A more in-depth physical explanation why that specific range of mass flows is unstable is still missing. Different characteristics were investigated in order to find an explanation of these unstable mass flows, for instance gravitational pressure drop versus power characteristics, but none turned out to provide any insight unfortunately.

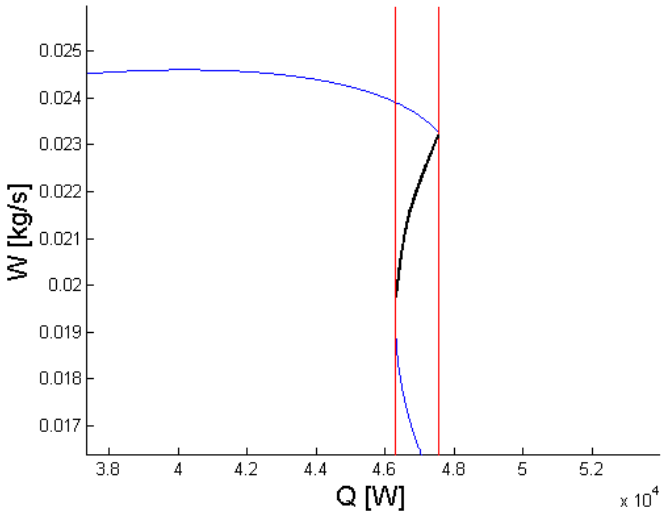

Figure 5.11: Flow rate versus power. The black line indicates the unstable flow rate for which Ledinegg instabilities can occur. The red lines indicate the region where more than one mass flow rate can exist for the same power input. N_{sub}=0.95, L_R=0 m and V_B=2 dm^3.

The range of unstable mass flows is calculated for every subcooling number and a stability map is derived in Figure 5.12a. At a first look the region overlaps quite well with the expected region and looks very similar to the Ledinegg unstable region found by Guido et al. (1991) for a single boiling water channel. However, the overlap is not perfect. Further investigation by overlapping the two stability maps showed that the Ledinegg unstable region also overlaps a part of the stable region and therefore there are also some mass flow rates indicated by the black line in Figure 5.11 which are apparently stable. A clear example of such a deviation is given in Figure 5.12b. This figure shows the overlap of the Ledinegg unstable region with the stability map shown in Figure 5.3. To make sure that mass flow rate versus power characteristics calculated by *Matlab* are correct they were also calculated with *Maple,* which solves the problem analytically. These characteristics were the same and therefore it can be concluded that this approach can not give a decisive answer about the Ledinegg instabilities. It can give a good approximation of where the Ledinegg unstable region must lie, but not the exact position of its boundaries.

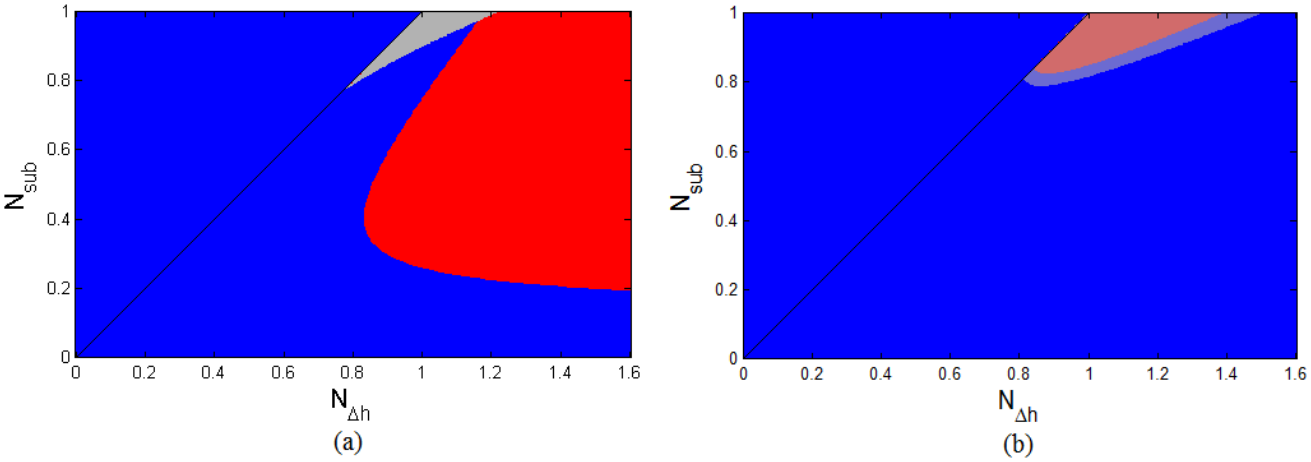

Figure 5.12: (a) Stability map plotted with the Ledinegg instabilities in gray, the unstable and stable region is indicated with red and blue respectively. V_B=2 dm^3, L_R=0 m. (b) Overlay of the stability map in Figure 5.3 with the Ledinegg unstable region. The Ledinegg unstable region also overlaps a part of the stable region. The black line indicates the N_{sub}=$N_{\Delta h}$ line.

Furthermore, the frequency maps of the stability maps can give additional information about the Ledinegg instabilities. As mentioned in section 4.4, at some operating conditions more than one mass flow rate can exist. For some combinations of N_{sub} and $N_{\Delta h}$ the mass flow is unstable and can then shift to a more stable one without any oscillations occurring. These instabilities are non-dynamic. Figure 5.13 shows the frequency map of the stability plot in Figure 5.12a and as can be seen, the presumed Ledinegg unstable region has zero frequency. Therefore, the frequency map supports the presumption that Ledinegg instabilities are present.

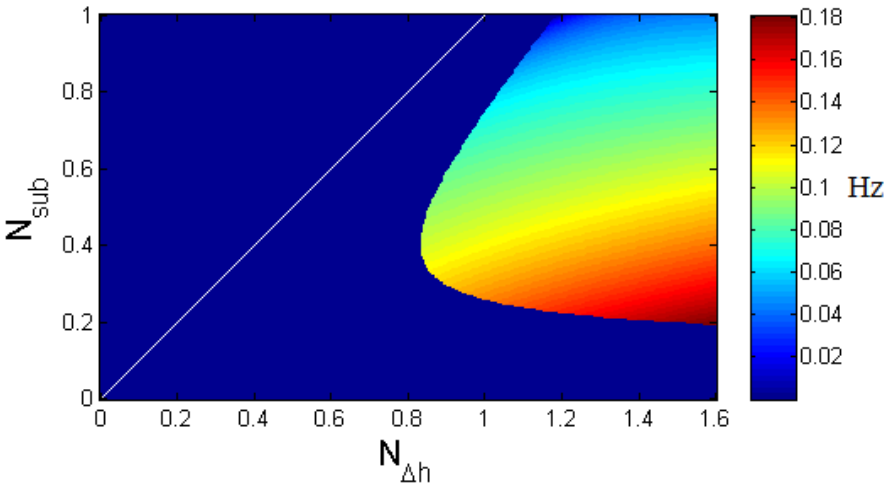

Figure 5.13: Frequency (Hz) map of stability map in Figure 5.10b. The Ledinegg unstable region in the stability map of Figure 5.12a has zero frequency.

Finally, the frequency maps of some stability maps indicate that there is a large region of non-dynamic instabilities in the unstable region, see Figure 5.14b. The system is destabilized with a smaller buffer vessel and a higher outlet pressure loss coefficient. The instability domain without frequencies is significantly large, however not all the instabilities are caused by Ledinegg instabilities. The relatively large unstable domain without frequencies is not entirely composed of Ledinegg instabilities as can be seen in Figure 5.14a, but are caused by another type of non-dynamic instabilities. What kind of instabilities these are remains unclear in this research. Furthermore, an instability domain arises above the $N_{sub}=N_{\Delta h}$ line where the low heating model applies. This domain has low frequencies and could possibly be Type-I instabilities.

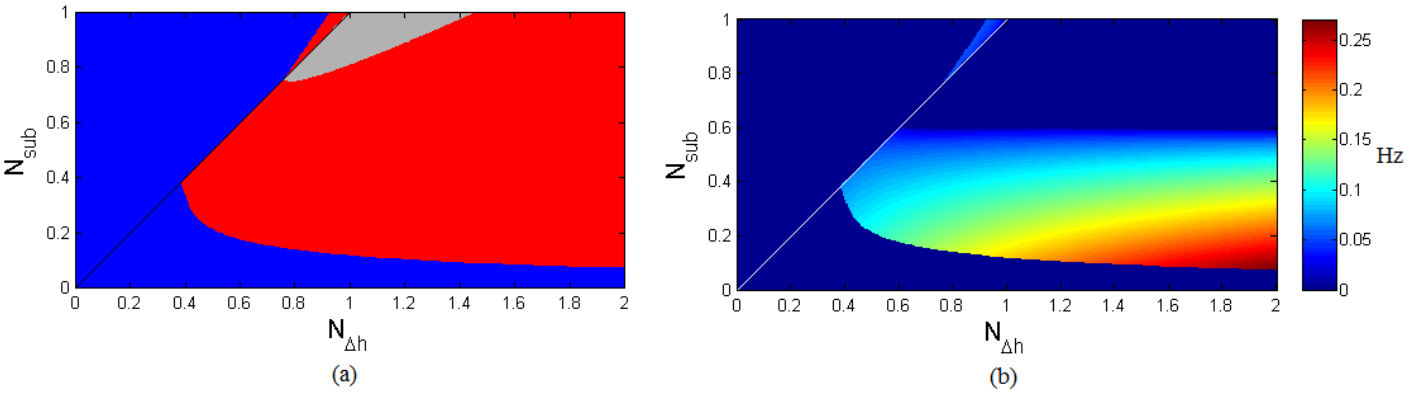

Figure 5.14: (a) Ledinegg instabilities indicated with gray, unstable region and stable region indicated with red and blue respectively. V_B=1 dm^3, K_R=40. (b) Frequency (Hz) stability map. A large instability domain without frequency arises, which does not entirely consists of Ledinegg instabilities. The black line and white line indicate the $N_{sub}=N_{\Delta h}$ line in both plots.

6 CONCLUSIONS

6.1 CONCLUSIONS

A linear stability analysis of a supercritical water loop driven by natural convection was performed with the use of a simplified mathematical model in which basic conservation balances apply. From this analysis qualitative results were obtained rather than quantitative ones. A parametric study was performed to investigate the influence of various design parameters of the loop. It is found that the volume of the buffer vessel has a significant stabilizing effect on the mass flow, because it acts like an attenuator that reduces the amplitudes of oscillations from introduced perturbations. However, the buffer vessel is unable to prevent the occurrence of Ledinegg instabilities. Even for a large volume of the buffer vessel the Ledinegg unstable region remains. Another result which is worth notifying is the influence of the length of the riser. Reactors driven by natural convection depend on a riser which is long enough to drive the circulation by natural convection. At the same time adding a riser does have consequences for the stability of the system. The parametric study showed that increasing the length of the riser destabilizes the system by introducing Type-I instabilities which are driven by a gravitational pressure drop. A long riser does increase the mass flow rate though and it is therefore important during the design of a HPLWR driven by natural convection that the trade-off between a sufficient mass flow rate and a stable system must be considered carefully.

Furthermore, by investigating the frequency domain of the stability map more insight into the nature of the instabilities can be acquired. Various domains exist in the stability map with different frequencies. A distinction has been made between two domains of different frequency. The relative low frequency region can be an indication of Type-I instabilities, which are driven by the gravitational pressure drop. And the higher frequency domain in the lower right part of the stability map (region around N_{sub}=0.6 and $N_{\Delta h}$=1.8 for the reference case) can be an indication of instabilities driven by the frictional pressure drop, Type-II instabilities. Also instabilities with zero frequency (i.e. non-dynamic instabilities) could give an indication of where Ledinegg instabilities occur. The important thing to remember is that the frequency maps can give insight into the type of instabilities and are a tool to further investigate the stability maps, but do not necessarily determine stand-alone the type of instabilities occurring in the system. Further investigation of the behavior of the NSB to changing design parameters and study of the conservation balances must be done in order to give conclusive results.

Finally, a method is proposed to investigate the occurrence of Ledinegg instabilities. Ledinegg instabilities can not be found by investigating the pressure versus mass flow rate characteristics of the water loop against the characteristic of the pump as is done by Ortega Gómez (2009). The water loop in this study is driven by natural convection and another method to find Ledinegg instabilities is required. Therefore the mass flow rate versus power characteristics are investigated to see if there are power inputs for which more than one mass flow rate can exist. An unstable mass flow rate could then change to another mass flow rate when the system is perturbed. This method does give a good indication of where the Ledinegg instabilities occur, but unfortunately it can not predict the Ledinegg instabilities

perfectly. More research should be done to refine this method and to offer a more in-depth physical explanation of the unstable mass flows in the mass flow rate versus power characteristics.

6.2 DISCUSSION

During the project assumptions and simplifications were applied to solve the stability problem and choices had to be made for the computational implementation. A part of these decisions are discussed here for their validity and solutions are proposed for further research if possible.

First of all, in this research a crude two-region approximation was used for the equation of state. This required that the core had to split up in two different nodes for one model. This approximation was visible in the stability map with a sharp transition at the $N_{sub}=N_{\Delta h}$ line. At this line the transition from one model to the other model occurs and the linearization of the equation of state has a discontinuous jump at this point. A better approximation can be done by introducing an approximation which is divided into more segments and follows the equation of state more closely. This would require a split up of the core into more nodes. A discontinuous jump would still be present, but the jump should be less rigorous.

Secondly, during the linearization the term $\underset{\sim}{x}_i \frac{d}{d\underset{\sim}{t}} \underset{\sim}{x}_j$ was present in the conservation balances and was chosen to be neglected. However, large perturbations can make these terms having a significant contribution in the balances. Not neglecting these would require a non-linear solving method, which lies out of the scope of this thesis, but might be worth looking at.

Thirdly, there is some room for improvement in the calculation of the Darcy friction factor. Currently these friction factors are calculated with a rather crude approximation without taken into account the differences between the properties of the different nodes in the water loop. For instance, the hydraulic diameter of each channel is the same and the roughness of the inner wall of the channels is not taken into account. Furthermore, the dynamic viscosity present in the Reynolds number is considered constant. The dynamic viscosity is actually a property of water and depends on the temperature. Refinement of the friction factor could lead to more correct stability maps.

Finally, this research can be extended by introducing neutronic-thermo-hydraulic coupling to the model. In this research the power is taken constant, but in an actual HPLWR the water would act as a coolant as well as a moderator. The mass flow rate would then have an influence on the power of the core and vice versa. The stability map could therefore look a lot different.

BIBLIOGRAPHY

Ambrosini, W. (2011). Assessment of flow stability boundaries in a heated channel with different fluids at supercritical pressure. *Annals of Nuclear Energy 38*, 615–627.

Ambrosini, W., & Sharabi, M. (2008). Dimensionless parameters in stability analysis of heated channels. *Nuclear Engineering and Design 238-8*, 1917-1929.

Boure, J., Bergles, A., & Tong, L. (1973). Review of two phase flow instability. *Nuclear Engineering and Design 25*, 165-192.

Chatoorgoon, V. (2001). Stability of supercritical fluid flow in a single-channel natural-convection loop. *International Journal of Heat and Mass Transfer 44*, 1963-1972.

Chatoorgoon, V., Voodi, A., & Fraser, D. (2005a). The stability boundary for supercritical flow in natural convection loops Part I: H2O studies. *Nuclear Engineering and Design 235*, 2570–2580.

Chatoorgoon, V., Voodi, A., & Upadhye, P. (2005b). The stability boundary for supercritical flow in natural-convection loops Part II: CO2 and H2. *Nuclear Engineering and Design 235*, 2581–2593.

Fischer, K., Schulenberger, T., & Laurien, E. (2009). Design of a supercritical water-cooled reactor with a three-pass core arrangement. *Nuclear Engineering and Design 239*, 800-812.

Guido, G., Converti, J., & Clausse, A. (1991). Density-wave oscillations in parallel channels - an analytical approach. *Nuclear Engineering and Design 125*, 121-136.

Jain, P., & Rizwan-Uddin. (2008). Numerical analysis of supercritical flow instabilities. *Nuclear Engineering and Design 238-8*, 1947-1957.

Janssen, L., & Warmoeskerken, M. (1997). *Transport phenomena Data Companion* (3rd ed.). VSSD.

Kam, F. (2011). *Development of a one-dimensional model for the stability analysis of a natural circulation Super Critical Water Reactor, M.Sc. Thesis.* Delft: TUDelft.

Koren, G. (2010). *Linear Stability Analysis of a Supercritical Water Loop driven by Natural Convection, B.Sc. Thesis.* Delft.

Lomperski, S., Cho, D., Jain, R., & Corradini, M. (2004). Stability of a natural circulation loop with a fluid heated through thermodynamic pseudo-critical point. *Proceedings of the 2004 International Congress on Advances in Nuclear Power Plants, ICAPP'04*, 1736-1741.

Marcel, C., Rohde, M., Masson, V., & Van der Hagen, T. (2009). Fluid-to-fluid modeling of supercritical water loops for stability analysis. *International Journal of Heat and Mass Transfer 52*, 5046–5054.

Matlab. (2013). *Function Reference*. (T. Mathworks, Producer) Retrieved from Mathworks: http://www.mathworks.nl/help/matlab/functionlist.html

NIST. (2011). *Thermophysical Properties of Fluid Systems*. Retrieved from The National Institute of Science and Technology: http://webbook.nist.gov/chemistry/fluid/

Ortega Gómez, T. (2009). *Stability analysis of the High Performance Light Water Reactor, Phd Thesis.* Institute for Nuclear and Energy Technology.

Papini, D., Cammin, A., Colombo, M., & Ricott, M. (2012). Time-domainlinearandnon-linearstudiesondensitywaveoscillations. *Chemical EngineeringScience 81*, 118-139.

Schulenberg, T., Starflinger, J., Marsault, P., Bittermann, D., Maráczy, C., Laurien, E., . . . Toivonen, A. (2011). European supercritical water cooled reactor. *Nuclear Engineering and Design 241-9*, 3505–3513.

Sharma, M., Pilkhwala, D., Vijayana, P., Sahaa, D., & Sinha, R. (2010). Steady state and linear stability analysis of a supercritical water natural circulation loop. *Nuclear Engineering and Design 240*, 588–597.

Spoelstra, J. (2012). *Numerical stability analysis of natural circulation driven supercritical water reactors, M.Sc. Thesis.* Delft: TU Delft.

Starflinger, J. (2010). *Public Final Report Assessment of the HPLWR Concept.* Germany.

T'Joen, C., & Rohde, M. (2012). Experimental study of the coupled thermo-hydraulic-neutronic. *Nuclear Engineering and Design 242*, 221-231.

Van Bragt, D. (1998). *Analytical Modeling of Boiling Water Reactor Dynamics.* Delft: Department of Reactor Physics of the Interfaculty Reactor Institute.

Wolfram. (2013). *9.1 Generalized Eigenvalue Problem*. Retrieved from Wolfram Mathematica: reference.wolfram.com/legacy/applications/anm/GeneralizedEigenvalueProblem/9.1.html

Appendices

APPENDIX A

Derivation of the momentum balance for the high heating model

With the use of the drawing in Figure A.1 the momentum balance is derived for the entire loop. The diameter of the pipe is constant as well as the area. The angle θ is defined as the angle of the cylinder axis in the flow direction with the positive z-axis, the positive z-axis is directed in the opposite direction of the gravity. The integration is taken along the whole loop and therefore the terms representing the transportation of momentum and the pressure difference can be taken as zero. Furthermore, because the loop is not continuous but divided into five nodes the integrations becomes a sum over every node.

$$dz\frac{dA\rho_z u_z}{dt} = A\rho uu\Big|_z - A\rho uu\Big|_{z+dz} + Ap_z - Ap_{z+dz} + \int_S \tau_{w\to f}\,dzdS - Adz\rho_z g\cos(\theta)$$

$$A\frac{dW}{dt} = A\frac{A\rho uu\Big|_z - A\rho uu\Big|_{z+dz}}{dz} + A^2\,\frac{p_z - p_{z+dz}}{dz} + A\int_S \tau_{w\to f}\,dS - A^2\rho_z g\cos(\theta)$$

$$A\frac{dW}{dt} = -\frac{d}{dz}\frac{W^2}{\rho_z} - A^2\,\frac{dp_z}{dz} + A\int_S \tau_{w\to f}\,dS - A^2\rho_z g\cos(\theta)$$

$$A\oint_{loop}\frac{dW}{dt}dz = -\cancel{\oint_{loop}\frac{d}{dz}\frac{W^2}{\rho_z}dz} - A^2\cancel{\oint_{loop}\frac{dp_z}{dz}dz} + A\oint_{loop}\int_S \tau_{w\to f}\,dSdz - A^2 g\oint_{loop}\rho_z\cos(\theta)dz$$

$$A\oint_{loop}\frac{dW}{dt}dz = -\tfrac{1}{2}A\oint_{loop}\left(\frac{f_z}{D_h} + K_i\delta\left(z - z_i\right)\right)\frac{W_z^2}{\rho_z}dz - A^2 g\oint_{loop}\rho_z\cos(\theta)dz$$

$$A\sum_i \frac{d}{dt}W_i L_i = -\tfrac{1}{2}\sum_i\left(\frac{f_i L_i}{D_h} + K_i\right)\frac{W_i^2}{\rho_i} - A^2 g\sum_{i\{0,1,R\}}\rho_i L_i + A^2 g\rho_{IN}L_D$$

Summation over each node leads to the following end result:

$$I: A\frac{d}{dt}W_0L_0 + A\frac{d}{dt}W_1L_1 + AL_R\frac{d}{dt}W_R + \frac{d}{dt}V_B W_0 + AL_D\frac{d}{dt}W_0 =$$
$$-\frac{1}{2}\left(\frac{f_0L_0}{D_h} + K_0\right)\frac{W_0^2}{\rho_0} - \frac{1}{2}\left(\frac{f_1L_1}{D_h} + K_1\right)\frac{W_1^2}{\rho_1} - \frac{1}{2}\left(\frac{f_RL_R}{D_h} + K_R\right)\frac{W_R^2}{\rho_R} - \frac{1}{2}\left(\frac{f_DL_D}{D_h} + K_D\right)\frac{W_0^2}{\rho_{IN}}\ldots$$
$$\ldots - A^2g\rho_0L_0 - A^2g\rho_1L_1 - A^2g\rho_RL_R + A^2g\rho_{IN}L_D$$

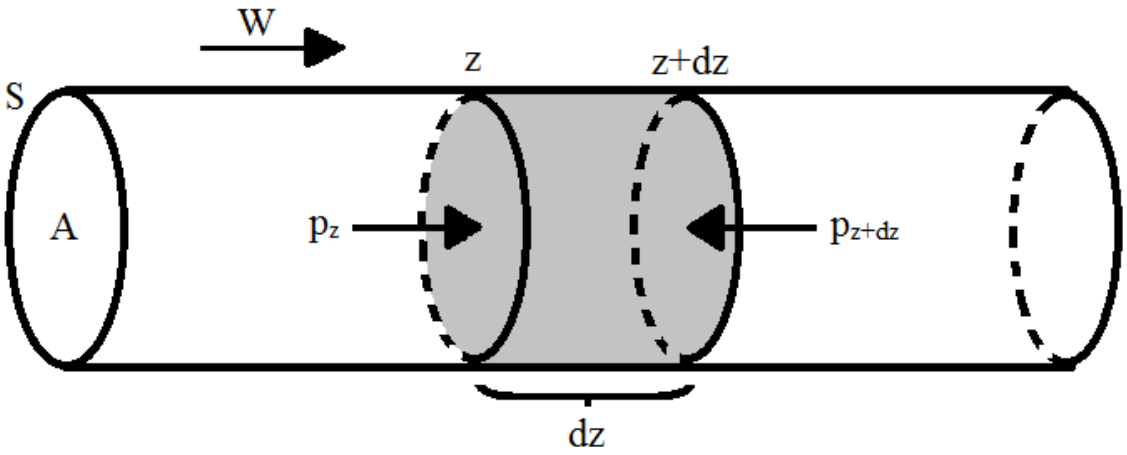

Figure A.1: Drawing of pipe flow used to derive the momentum balance.

Taylor expansion

The following Taylor expansion is used in chapter 2 to linearize the specific volume and density.

$$f(x)\big|_a \approx f(a) + \frac{f'(a)}{1!}(x-a) + \frac{f''(a)}{2!}(x-a)^2 + \frac{f^{(3)}(a)}{3!}(x-a)^3 + \ldots \qquad \text{(A.1)}$$

APPENDIX B

High heating model: Coefficient matrices

Coefficient Matrix *A* **Coefficient Matrix *B* →**

$$
\begin{array}{c}
\\
\underset{\sim}{M}_0 \\
\underset{\sim}{M}_1 \\
\underset{\sim}{M}_R \\
\underset{\sim}{E}_1 \\
\underset{\sim}{E}_R \\
\underset{\sim}{I}
\end{array}
\begin{pmatrix}
\rho_0\left(\dfrac{\underset{\sim}{H}_0}{h_{pc}}-1\right) & 0 & 0 & 0 & 0 & 0 \\
\dfrac{1}{\bar{\upsilon}_1}-\dfrac{\underset{\sim}{H}_0}{h_{pc}}\rho_0 & -\dfrac{\bar{L}_1 N_{\Delta h} C_1 h_{pc}}{\upsilon_{pc}\bar{\upsilon}_1^2} & 0 & 0 & 0 & 0 \\
0 & 0 & -\dfrac{\underset{\sim}{L}_R N_{\Delta h} C_1 h_{pc}}{\upsilon_{pc}\bar{\upsilon}_R^2} & 0 & 0 & 0 \\
\dfrac{\bar{H}_1}{\bar{\upsilon}_1}-\underset{\sim}{H}_0\rho_0 & \dfrac{\bar{L}_1}{\bar{\upsilon}_1}\left(1-\dfrac{N_{\Delta h} C_1 h_{pc}\bar{H}_1}{\upsilon_{pc}\bar{\upsilon}_1}\right) & 0 & 0 & 0 & 0 \\
0 & 0 & \dfrac{\bar{L}_R}{\bar{\upsilon}_R}\left(1-\dfrac{N_{\Delta h} C_1 h_{pc}\bar{H}_R}{\upsilon_{pc}\bar{\upsilon}_R}\right) & 0 & 0 & 0 \\
0 & 0 & 0 & 1-\bar{L}_1+L_D+\bar{V}_B & \bar{L}_1 & \underset{\sim}{L}_R
\end{pmatrix}
\begin{array}{c}
\\
\underset{\sim}{M}_0 \\
\underset{\sim}{M}_1 \\
\underset{\sim}{M}_R \\
\underset{\sim}{E}_1 \\
\underset{\sim}{E}_R \\
\underset{\sim}{I}
\end{array}
\begin{pmatrix}
w_0 & w_1 & w_R \\
h_1 & h_R & \\
l_1 & &
\end{pmatrix}
$$

$$
\begin{array}{c}
\\
\underset{\sim}{M}_0 \\
\underset{\sim}{M}_1 \\
\underset{\sim}{M}_R \\
\underset{\sim}{E}_1 \\
\underset{\sim}{E}_R \\
\underset{\sim}{I}
\end{array}
\begin{pmatrix}
\dfrac{1}{h_{pc}} & 0 & 0 & 1-\dfrac{\underset{\sim}{H}_{IN}}{h_{pc}} & 0 & 0 \\
-\dfrac{1}{h_{pc}} & 0 & 0 & \dfrac{\underset{\sim}{H}_{IN}}{h_{pc}} & -1 & 0 \\
0 & 0 & 0 & 0 & 1 & -1 \\
0 & -1 & 0 & \underset{\sim}{H}_{IN} & -\bar{H}_1 & 0 \\
0 & 1 & -1 & 0 & \bar{H}_1 & -\bar{H}_R \\
\dfrac{1}{2}\left(\dfrac{f_0\underset{\sim}{\upsilon}_0}{D}-\dfrac{f_1\bar{\upsilon}_1}{D}\right)+\dfrac{1}{\upsilon_0 N_{Fr}}-\dfrac{1}{N_{Fr}\bar{\upsilon}_1} & -\dfrac{1}{2}\left(\dfrac{f_1\bar{L}_1}{D}+K_1\right)+\dfrac{\bar{L}_1}{\bar{\upsilon}_1^2 N_{Fr}}\dfrac{N_{\Delta h} C_1 h_{pc}}{\upsilon_{pc}} & -\dfrac{1}{2}\left(\dfrac{f_R\underset{\sim}{L}_R}{D}+K_R\right)+\dfrac{\underset{\sim}{L}_R}{\bar{\upsilon}_R^2 N_{Fr}}\dfrac{N_{\Delta h} C_1 h_{pc}}{\upsilon_{pc}} & -\left(\left(\dfrac{f_0\underset{\sim}{L}_0}{D}+K_0\right)\underset{\sim}{\upsilon}_0+\left(\dfrac{f_D\underset{\sim}{L}_D}{D}+K_D\right)\underset{\sim}{\upsilon}_{IN}-\underset{\sim}{\upsilon}_{IN}\right) & -\left(\dfrac{f_1\bar{L}_1}{D}+K_1\right)\bar{\upsilon}_1 & -\left(\dfrac{f_R\underset{\sim}{L}_R}{D}+K_R+\dfrac{\underset{\sim}{\upsilon}_{IN}}{\bar{\upsilon}_R}\right)\bar{\upsilon}_R
\end{pmatrix}
\begin{array}{c}
\\
\underset{\sim}{M}_0 \\
\underset{\sim}{M}_1 \\
\underset{\sim}{M}_R \\
\underset{\sim}{E}_1 \\
\underset{\sim}{E}_R \\
\underset{\sim}{I}
\end{array}
\begin{pmatrix}
0 & 0 \\
0 & 0 \\
-1 & 0 \\
0 & -\bar{H}_R \\
\bar{H}_1 & \\
w_1 & w_R
\end{pmatrix}
$$

$$
\begin{array}{c}
\\
\underset{\sim}{M}_0 \\
\underset{\sim}{M}_1 \\
\underset{\sim}{M}_R \\
\underset{\sim}{E}_1 \\
\underset{\sim}{E}_R \\
\underset{\sim}{I}
\end{array}
\begin{pmatrix}
0 & 0 & 0 & 0 & 0 & 0 \\
0 & 0 & 0 & 0 & 0 & 0 \\
0 & 0 & 0 & 0 & 0 & 0 \\
0 & 0 & 0 & 0 & 0 & 0 \\
0 & 0 & 0 & 0 & 0 & 0 \\
1 & 0 & 0 & 0 & 0 & 0
\end{pmatrix}
\begin{array}{c}
\\
\underset{\sim}{M}_0 \\
\underset{\sim}{M}_1 \\
\underset{\sim}{M}_R \\
\underset{\sim}{E}_1 \\
\underset{\sim}{E}_R \\
\underset{\sim}{I}
\end{array}
\begin{pmatrix}
w_0 & w_1 & w_R \\
h_1 & h_R & \\
l_1 & &
\end{pmatrix}
$$

Low heating model: Coefficient matrices

Coefficient Matrix *A*

$$
\begin{array}{c}
\\
\underset{\sim}{M}_0 \\
\underset{\sim}{E}_0 \\
\underset{\sim}{E}_1 \\
\underset{\sim}{I}
\end{array}
\begin{pmatrix}
\frac{1}{2}C_1 N_{\Delta h} h_{pc} \nu_{pc} & C_1 N_{\Delta h} h_{pc} \nu_{pc} \underset{\sim}{L}_R & 0 & 0 \\
\frac{1}{2}\overline{\underset{\sim}{\rho}}_0 + \frac{1}{2}C_1 N_{\Delta h} h_{pc} \nu_{pc} \overline{\underset{\sim}{H}}_0 & C_1 N_{\Delta h} h_{pc} \nu_{pc} \overline{\underset{\sim}{H}}_{out} \underset{\sim}{L}_R & 0 & 0 \\
0 & \underset{\sim}{L}_R \overline{\underset{\sim}{\rho}}_R + \underset{\sim}{L}_R C_1 N_{\Delta h} h_{pc} \nu_{pc} \left(\overline{\underset{\sim}{H}}_R - \overline{\underset{\sim}{H}}_{out} \right) & 0 & 1 + \underset{\sim}{L}_D + \overline{\underset{\sim}{V}}_B \quad \underset{\sim}{L}_R \\
0 & 0 & \underset{\sim}{h}_R & \underset{\sim}{w}_R
\end{pmatrix}
\begin{array}{c}
\\
\\
\\
\\
\underset{\sim}{h}_{out} \quad \underset{\sim}{w}_0
\end{array}
$$

Coefficient Matrix *B* →

$$
\begin{array}{c}
\\
\underset{\sim}{M}_0 \\
\underset{\sim}{E}_0 \\
\underset{\sim}{E}_R \\
\underset{\sim}{I}
\end{array}
\begin{pmatrix}
0 & 0 & 1 & -1 \\
-1 & 0 & \underset{\sim}{H}_{IN} & -\overline{\underset{\sim}{H}}_{out} \\
1 & -1 & 0 & \overline{\underset{\sim}{H}}_{out} - \overline{\underset{\sim}{H}}_R \\
\frac{1}{2}\left(\left(\frac{f_0}{\underset{\sim}{D}} + K_0 \right) \frac{1}{\overline{\underset{\sim}{\rho}}_0^{\,2}} - \frac{1}{N_{Fr}} \right) C_1 N_{\Delta h} h_{pc} \nu_{pc} & \frac{1}{2}\left(\left(\frac{f_R \underset{\sim}{L}_R}{\underset{\sim}{D}} + K_R \right) \frac{1}{\overline{\underset{\sim}{\rho}}_R^{\,2}} - \frac{\underset{\sim}{L}_R}{N_{Fr}} \right) C_1 N_{\Delta h} h_{pc} \nu_{pc} & \left(\upsilon_{IN} - \left(\frac{f_0}{\underset{\sim}{D}} + K_0 \right) \overline{\underset{\sim}{\upsilon}}_0 \right) & -\left(\left(\frac{f_R \underset{\sim}{L}_R}{\underset{\sim}{D}} + K_R \right) \overline{\underset{\sim}{\upsilon}}_R + \upsilon_{IN} \right)
\end{pmatrix}
\begin{array}{c}
\\
\\
\\
\\
\underset{\sim}{h}_{out} \quad \underset{\sim}{h}_R \quad \underset{\sim}{w}_0 \quad \underset{\sim}{w}_R
\end{array}
$$